Research Square

Preprints are preliminary reports that have not undergone peer review.
They should not be considered conclusive, used to inform clinical practice,
or referenced by the media as validated information.

Vertical characteristics of storms on different horizontal extent and reflectivity thresholds over the west coast of India in 2024 during the pre-monsoon and monsoon seasons using C-band radar, INSAT-3D, and reanalysis data

Shailendra Kumar

shailendrak89@gmail.com

Vikram Sarabhai Space Centre

Research Article

Keywords: C-band, Radar reflectivity, Monsoon, INSAT, pre-monsoon, Storm intensity

Posted Date: November 25th, 2026

DOI: https://doi.org/10.21203/rs.3.rs-11718308/v1

License: This work is licensed under a Creative Commons Attribution 4.0 International License.
Read Full License

Additional Declarations: No competing interests reported.

Vertical characteristics of storms on different horizontal extent and reflectivity thresholds over the west coast of India in 2024 during the pre-monsoon and monsoon seasons using C-band radar, INSAT-3D, and reanalysis data

Shailendra Kumar*

Shailendra Kumar: shailendrak89@gmail.com

Space Physics Laboratory

Vikram Sarabhai Space Centre, Trivandrum

Kerala, India, 695022

Keywords: C-band, Radar reflectivity, Monsoon, INSAT, pre-monsoon, Storm intensity

Abstract

The vertical profile of radar reflectivity (VPRR) approach is applied to investigate storm intensity across different horizontal scales and at different radar reflectivity (Ze) thresholds from pre-monsoon to monsoon months in 2024 over Thumba using C-band radar. It is observed that the vertical structure of the Ze depends on the horizontal scales and Ze thresholds used in the present study. For example, irrespective of storm size (horizontal extent), the Ze is highest near the surface (~2-3 km altitude) and then decreases rapidly with altitude. However, at smaller horizontal scales, Ze peaks at higher altitudes and then decreases with altitude. It is observed that pre-monsoon storms are more intense than monsoon storms, and the intensity difference is smaller at smaller horizontal scales. Within a few months, intense storm activity can develop at small scales with convective intensity similar to other months, when intense storm activity develops only at large horizontal scales. Large-scale storms show greater differences below 4 km altitude than smaller-scale storm activity. On a monthly basis, March- and April-based storms are more vertically intense (higher Ze at higher altitudes) and have greater precipitation echo top heights (ETHs), followed by May and June, though with lower frequency. Pre-monsoon months have more intense individual precipitation hotspots (Ze> 35 dBZ) than monsoon months, and occur over land-dominated areas rather than oceanic ones. July-to September have the weakest and shallower storms (fewer Ze and ETHs). The frequency of intense storms decreases rapidly above 4 km altitude in May and June as the horizontal extension increases; e.g., there is a higher chance in IIVP_storm for the vertically extended and the least and medium horizontal extensions. During the monsoon months, IIVP_storm can be vertically extended, with greater horizontal extension than in the pre-monsoon months, above 9 km altitude. The presence of the Western Ghats (WGs) in the study region strongly affects storm precipitation characteristics, with more severe storms observed on the windward side of the WGs. The reanalysis data reveal that severe storms are linked with moderate Convective Available Potential Energy (CAPE) and thermodynamic indices, especially during the

monsoon months. Numerical modeling of these observations will be the next step to examine how dynamics and thermodynamic features are associated with severe storms across different seasons. The present results provide a quantitative assessment of the vertical structure of storms over Thumba from pre-monsoon to monsoon months, using DWR observations from 2024 for the first time.

1. Introduction

Precipitation systems are organized at various horizontal and vertical scales, starting from individual Cumulonimbus clouds (Cb<~5-10 km; Heymsfield et al. 2010), to storms and then into meso-scale convective systems (MCSs; ~100 Km, Houze 2004). Their vertical structure and intensity vary from location to location and across seasons worldwide (Pertson and Rutledge 2001; Xu and Zipser 2012; Kumar and Silva 2019, 2020, 2024a). It is also observed that MCSs are embedded with many storms, which themselves consist of several individual Cb clouds or cumulus congestus clouds (Houze 2004; Sindhu and Bhat 2018). These storms are associated with heavy precipitation and lightning activity, and they occupy 30-70% of convective areas within MCSs and contribute to more than 90% of convective precipitation within MCSs (Feng et al. 2007). Kumar et al. (2019a) showed that surface rainfall within MCSs depends on their top heights, intensity, and horizontal extent, and revealed the storm-scale importance of their hierarchy (Liu and Zipser 2015). These convective storms are responsible for severe weather systems and play an important role in stratosphere-troposphere exchange processes (Subrahmanmyam and Kumar 2023a), where they are associated with intense updrafts, the growth of frozen hydrometeors, and lightning activity (Sindhu and Bhat 2017; Jha et al. 2025). Recognizing the importance of convective storms, numerous studies have investigated them using ground-based radar (e.g., Cifelli et al., 2002; Kumar et al., 2005; Uma and Rao, 2009; Uma and Sama, 2025).

Potts et al. (2000) studied 30-dBZ storms over Australia during the summers of 1995 and 1996 and found that 64% of storms had an area of less than 103 km2. Caine et al. (2013) studied the relationship between storm lifespan and storm top height across various radar reflectivity thresholds. Novo et al. (2014) showed that storms of 25 dBZ lie between 2 and 18 km altitudes over Cuban regions; however, storms of 45 dBZ, with a minimum volume of 100 km3, peak at ~6 km altitude. Sindhu and Bhat (2018) also used C-band polarimetric radar data to explore storm characteristics over Delhi and observed that more than 80% of 30-dBZ storms have a lifespan of less than 1 hour, that storm areas are less than 100 km2, and that echo top heights lie between 6 and 10 km. Sindhu and Bhat (2021) showed that in the northern land areas of India, storms move faster in the pre-monsoon season than in the monsoon season. Subrahmanmyam and Kumar (2023b) used C-band radar data to investigate organized precipitation bands over tropical regions during the monsoon seasons. The results showed that blocking effects induced by the Western Ghats (WGs) around the radar site play a key role in the formation of organized precipitation bands. Subrahmanmyam and Kumar (2023a) observed the deep convective cell characteristics during the monsoon seasons and showed that the occurrences of reflectivities in the range of 25-35 dBZ dominate below 6 km, whereas the reflectivity in the range of 10–20 dBZ dominates above 6 km. The occurrence of 40 dBZ tops in radar echoes peaks in the early morning and late night

over the ocean, and in the afternoon and late night over land regions. It is observed that most storm areas lie within a few hundred km^2, with heights ranging from 2 km to 18 km, and that the average lifespan is around ½ to 1 h across different tropical locations (Sindhu and Bhat 2018; Uma and Sama 2024).

Deep convection is intermittent during the pre-monsoon period, moistens the middle atmospheric layers, and stratiform clouds occur during the monsoon period (Krishnakumar et al. 2009; Kumar 2026). The mid-atmospheric layers are observed to be dry prior to monsoon onset and were consistently moistened as the low-level jet (LLJ) intensified. The monsoon onset is characterized by significant changes in the large-scale circulation and the associated rainfall distribution over the Indian landmass (Findlater, 1969). During the pre-monsoon period, there are light westerly winds above the west coast from the surface to 800 hPa, while the onset stage of the monsoon is characterized by a sudden increase in daily precipitation, an increase in vertically integrated water vapor, and intensification of the low-level jet. Earlier studies have reported that the intensification of LLJ during the monsoon seasons and the heating of the mountain slope, which triggers convection, play key roles in the formation of precipitating systems over the mountain region (e.g., Gray and Jacobson, 1977; Subrahmanyam and Kumar, 2022). Jash et al. (2018) investigated the features of pre-monsoon thunderstorms and revealed that the percentages of convective and stratiform pixels were 22% and 78%, respectively over southern peninsular India. During the transition from the pre-monsoon to the monsoon period, changes in the thermal and mechanical characteristics of the atmosphere are more pronounced in the boundary layer (Gray and Jacobson, 1977). The high temperature and moisture availability make Kerala and parts of Karnataka and Tamil Nadu vulnerable to storms in the evening and late-night hours of the pre-monsoon period. The convective environment over the Indian subcontinent is markedly different during hot, dry pre-monsoon conditions than during the monsoon period. The orographic features play a vital role in the WGs, depending on whether they propagate from the landward or the oceanic side. Orography also plays a vital role, as WGs introduce our study regions, and the local convergence and large-scale subsidence are also important in the formation of thunderstorms and their rainfall intensity (Romatschke and Houze 2011a;b).

It is well known that monsoonal clouds are characterized by low-level clouds with limited vertical development due to a stable atmosphere resulting from the cooling effect of heavy precipitation (Mathew et al. 2021). Romatschke and Houze (2011a) showed that precipitation during pre-monsoon months is more convective and more sensitive to synoptic forcing. They showed that India's west coast consists of smaller systems that contribute to surface rainfall. During the monsoon season, higher moisture is advected from the AS towards the coastal areas, which can result in intense storms when they cross the coast, and WG results in intense orographic convection (Pisharoty 1965; Trenberth 1999; Swapna 2002). Recently, using the space-based cloud profiler radar, it was observed that the geographical locations of the different cloud systems depend on their horizontal extension and maximum vertical altitude over South Asia (Kumar 2024a). It motivates us to examine precipitation systems using a similar approach, drawing on ground-based observations from the pre-monsoon to the monsoon seasons, and to compare

them. Understanding the vertical structure of precipitating cloud systems across different horizontal and vertical scales is crucial for various practical applications, such as predicting natural hazards, estimating radiation, parametrization cumulus, and designing satellite payloads for measuring precipitation (Sindhu and Bhat 2018). The pre-monsoon season witnesses some of the most severe local thunderstorms near the foothills of the southwest coast (Romatschke and Houze 2011a, b; Das et al. 2014) that have the potential to cause landslides and flash floods. Comprehensive differences in storm vertical structure over Thumba remain poorly understood and must be investigated. Studying the vertical characteristics of storms over the ISM gateway is important for addressing rainfall variability and better representing these systems in regional and climate models. *Previous* studies rely on satellite-based observations with very poor spatial resolution (limited swath width) and focus on the Indian continent; the derived storm characteristics mainly cover the main monsoon zone, not southernmost peninsular India. Also, very limited studies are available on different weather conditions across India. The ground-based radar observations provide an excellent opportunity to compare storm rainfall intensity between the pre-monsoon and monsoon seasons. In the present study, we explored the C-band radar to investigate the vertical characteristics of precipitation at different horizontal scales. Three important questions are investigated in the present study and listed below:

1. How does the vertical structure of the precipitation vary at different horizontal scales over tropical locations during the pre-monsoon to monsoon months?

2. Differences in the storm's characteristics from the pre-monsoon months to the monsoon's end over the tropical locations?

3. How do the atmospheric thermodynamics and dynamical conditions affect the storm's vertical characteristics?

The present results provide a quantitative assessment of the vertical structure of precipitation at different horizontal scales over THUMBA using DWR observations.

2. Data and methodology

2.1. C-band radar

Present study uses high-resolution volumetric radar data the horizontal radar reflectivity factor (Ze) data from the C-band polarimetric Doppler weather radar (DWR, wavelength: 5.33 cm; frequency: 5.625 GHz; gain of anteena 45 dB) installed at Thumba, Trivandrum, India, located at the coast of the AS and flanked by the WGs on the east (Fig. 1). The radar is located in the Indian state of Kerala, which is known as the gateway of Indian Summer Monsoon (ISM) and is shown in Fig. 1 along with topographical features around the radar site. Detailed information on the C-band DWR is available in Subrahmanyam and Baby (2020). Kumar et al. (2020) calibrated the C-band radar observations using a metallic sphere to correct the radar-based Ze and observed a difference of 5.563 dB in the radar constant and 0.45 dBZ in the radar reflectivity. They also compared the C-band observations with the Global Precipitation Measurement (GPM) data, and both showed similar trends with minute differences (Kumar et al. 2020).

In the present study, we used the 3D volumetric gridded de-cluttered Ze data (Panda et al. 2018), obtained from the mosdac.gov.in. The Ze data used in the present study are corrected for clutter using a combination of a spatial continuity filter and a fuzzy-logic-based echo classification algorithm (Panda et al. 2018). The corrected Ze from all elevations is then gridded into a 3D volumetric grid having a resolution of 250 x 1 km x 1 km. The data is gridded at (81x481x481) with a horizontal resolution of (1 km x 1 km) and vertical resolution of (250 m), and the maximum altitude considered while gridding is 20.0 km. In the present study, a total of 273 days of round-the-clock DWR-based observations are considered from March to September in 2024 (each file is 400 MB).

2.2 Storms

The equivalent radar reflectivity factor (Ze) is the primary data provided by the radar which is proportional to the 6th power of hydrometeor size, considered as a proxy for hydrometeor concentration and rain rate (RR) in a precipitating cloud. Both Ze and RR are related as $Z=148*R^{1.55}$ for convective echoes. In the present study, a storm is considered a contiguous area of Ze with a minimum Ze threshold and area within the radar volume (Dixon and Wiener 1993; Sindhu and Bhat 2018, 2021). To obtain the detailed vertical structure of storms, we applied the VPRR (vertical profile of radar reflectivity) technique, which provides the vertical extent of storms across different horizontal scales (Lutz and Zipser 1994; Kumar and Bhat 2016). Importantly, we considered the storms at each half an hour. The data below 1 km altitude are likely to be contaminated by multiple reflections from the Earth's surface.

In this work, the intensity of a convective cell is defined by the maximum Ze observed at different attitudes. Nature favors the formation of individual, intense clouds that gather to form a storm, allowing them to develop with different horizontal extents and suit lateral entrainment; thus, several storm types are defined at different horizontal scales in the present study. The selection of storms consists of several steps and constraints on minimum storm area and Ze thresholds (Sindhu and Bhat 2018). First, we defined a cloud system by projecting the maximum Ze between 2 and 4 km altitude (composite Ze between 2 to 4 km altitude). The freezing height (0°C isotherm) lies at ~5 km altitude near the Thumba station, so setting the storms between 2 to 4 km altitude, will not be affected by the melting of snow near the bright band (Sindhu and Bhat 2018;2021). Only cloud systems that consist of at least one pixel with Ze>= 35 dBZ and at least 30 km^2 are considered storms here (Fig. 2a; Sindhu and Bhat 2018; Dixon and Wiener 1993). The 35 dBZ threshold is also used in earlier studies (e.g., Goudenhoofdt and Delobbe 2013; Kumar et al. 2013; May and Ballinger 2007; Peter et al. 2015; Utsav et al. 2017; Sindhu and Bhat 2018; Krishna et al. 2021; Jha et al. 2021, 2022). To avoid duplicate storms, the next storm is observed only after half an hour (Sindhu and Bhat 2018). Once the storms are defined, three types of vertical profiles are considered and as mentioned below.

a1. Vertical Profiles of Individual Storms (VP_storm):

Figure 2a shows the composite Ze between 2 and 4 km altitude. Here, two individual storms are observed, each with an area of connected Ze and at least one pixel with Ze> 35 dBZ. It also seems

that both storms are embedded in MCS, where an area of higher Ze (Ze_{max}) is trailed by the weaker Ze (Houze 1993). For each storm, we selected the maximum Ze at each altitude and generated vertical profiles of Ze_{max} for that storm, which we termed VP_storm. It shows how Ze_{max} varies across individual storms, regardless of their shapes, sizes, or orientations. A similar approach was previously applied to the satellite-based radar Ze to create vertical profiles of precipitation features (Nesbitt et al. 2006; Xu and Zipser 2012; Kumar 2016). Figure 2c shows an example of VP_storm used in the present study. VP_storm consists of the maximum Ze at each altitude (Xu and Zipser 2012; Kumar 2017), and reveals the maximum intensity at each altitude in the storm on a monthly basis.

a2. Individual Intense Vertical Profiles within the Storms (IIVP_storm):

Figure 2b shows the vertical cross-section (composite Ze) of both storms and reveals the vertical reach of Ze in two storms. It is observed that Storm B is more intense compared to Storm A, with its tops nearly penetrating the tropopause. It has a thin core (~10 km) of Ze extending beyond 12 km altitude with Ze>30 dBZ, and with Ze>35 dBZ extends between the 1 to 8 km altitudes, and is part of the Cb clouds (Guimond et al. 2010; Heymsfield et al. 2010; Bhat and Kumar 2015; Kumar and Bhat 2016). At the same time, there are many other/more intense convective precipitating cells that are also observed with Ze>35 dBZ, extending between 2 to 4 km altitudes, but overall they are not extending beyond 8 km altitude, and may belong to the shallower intense precipitating cells (Kumar and Bhat 2017; Kumar 2018). Within the storm-A, a precipitation top is observed below the 12 km altitude with a wide core (~15 km) of Ze>35 dBZ. These vertical cross sections show that, even at low levels with high Ze (>40 dBZ), it does not necessarily penetrate deeper into the atmosphere. Observations conducted prior to 1990 revealed that the width of updraft cores in tropical convective systems is typically less than ~5 km (LeMone and Zipser, 1980; Jorgensen and LeMone, 1989). Observations from a nadir-looking Doppler radar onboard an aircraft at an altitude of around 20 km showed an area of updraft width, defined as vertical velocity>5 ms-1, corresponding to 8-10 km over land, but over the ocean it has a width of 5-6 km only (Heymsfield et al. 2010; Guimond et al., 2010). Thus, the vertical cross-section captured in the present study can be considered an area of coherent updrafts or downdrafts with sizes nearly comparable to or larger than those of a grid pixel.

It is clearly observed that, within each individual storm, there are many individual Ze pixels are observed with Ze>35 dBZ (Fig. 2). Thus, considering only the maximum Ze at each altitude for each storm, will not be able to reveal the characteristics of vertical extensions/intensity of all theintense hotspots (Ze>35 dBZ; Liu and Zipser 2015; Kumar 2016). We applied the VPRR approach (Zipser and Lutz 1994) to capture all these individual intense vertical profiles embedded within the storms and termed them IIVP_storm as VPRR provides the most intense precipitating profiles in a given radar volume and is a classical approach to gain insight into the storm structure (Sindhu and Bhat 2018; Bhat and Kumar 2015; Lutz and Zipser 1994). The three important features of cloud/precipitating cells are: first, they can tilt; second, they can penetrate at different altitudes; and third, their horizontal extent is not identical; thus, the VPRR approach will consider these

limitations (Lutz and Zipser 1994; Donalsson 1961). Donalsson (1961) applied the aforementioned approach and demonstrated its importance for detecting tornadoes and hail in thunderstorms. Szoke et al. (1986) also applied a similar approach, observed major differences between the oceanic and mid latitude cells, and provided crucial information on higher-latitude regimes. They revealed that higher reflectivities in the mixed-phase and ice regions indicate larger hydrometeors (particles) and higher updraft speeds.

To construct the IIVP_storm, if a pixel with Ze>35 dBZ is observed, we select the maximum Ze from its nearest neighbor in all directions (Lutz and Zipser 1994; Donalsson 1961; Bhat and Kumar 2015). Once the pixels are used, all corresponding values are set to 0, and the process is repeated to find another Ze>35 dBZ based IIVP_storm. By repeating these processes, we extracted all the IIVP_storm embedded in each storm (Kumar and Bhat 2016). To assess the impact of cloud-top tilt and ETHs, we constructed the IIVP_storm at three horizontal scales: small (9-km^2), medium (25-km^2), and large (49-km^2). To construct the IIVP_storm at 9 km^2, we considered only the nearest grid cell to the central grid cell; for 25 km^2 and 49 km^2, we considered two and three nearest grid cells respectively. Figure 2d shows an example of IIVP_storm at 25 km^2 for the two storms shown in Figure 2a. Comparison of IIVP_storm across these three horizontal boxes ensures that if a cloud/precipitation cell is tilted and cannot be captured by the smaller grid box, it must be captured by the larger grid boxes. However, in the larger box, the adjacent cell must be intruded. The different grid boxes will provide information on how quickly intense rain hotspots degrade from pre-monsoon to the end of the monsoon months.

a3. Intense Vertical Profiles (IVPs):

From the horizontal and vertical composite Ze, it is clear that even when the composite Ze are nearly equal at altitudes of 2 and 4 km, their vertical extension (ETHs) is not identical (Subhryamanyam and Kumar 2023). For example, a few individual vertical profiles of Ze are deeper than other columnar Ze profiles, even when the Ze below the freezing level is lower or equal (Fig. 2b). Also, since Thumba is a coastal region and south of the WGs, the probability of shallower but intense clouds/precipitation would be higher in these regions (Kumar and Bhat 2017; Kumar 2018; Uma and Sama 2024). To investigate such profiles, which are both intense-deeper and intense-shallower, we classified intense vertical profiles (IVP) at altitudes of 3 and 8 km and termed them IVP3 and IVP8 (Kumar et al. 2024a). To draw the IVPs, the first step is to choose the 95th percentile of Ze (Ze^{95}) at altitudes of 3 and 8 km, and then draw the IVPs around the chosen Ze using the VPRR approach (Yuter and Houze 1995; Zipser 2006). Once the Ze^{95} is selected at 3 and 8 km, VPRR approach is applied on horizontal grid boxes at 5 km x 5 km to construct the IVPs (Fig. 2e and 2f). In the past Zipser and Lutz 1994 used 8 km × 8 km; Sindhu and Bhat 2018 used 10 km x 10 km to construct the IVPs. The different grid boxes will provide information on how quickly intense rain hotspots degrade horizontally from pre-monsoon to the end of the monsoon months. However, before starting to analyze the obtained profiles, we applied a few constraints on the vertical profiles:

c1. Connectivity (to remove multilayer clouds): The vertical profiles used in the present study must be connected by at least 5 dBZ. We have selected only the part of the profiles that started below 2 km altitude and ended at the altitude where Ze<5 dBZ. Above that altitude, we removed the Ze. Also, at least four connecting pixels with Ze>5 dBZ must exist in each vertical profile. It will help us remove multilayer clouds, upper-level noise, and intense cloud cells that develop only near the ground.

c2. Contributing (number of profiles reaching different altitudes): We plotted the average Ze only at altitudes that contain at least 90% Ze profiles across all samples. When calculating the average profiles, any altitude level with a sample size less than 5% of the maximum sample size across all altitude levels is omitted. This constraint will help us remove altitudes where the various vertical profiles do not significantly contribute to specific altitudes.

c3. Minimum echo top height: The ETHs of each vertical profile must be above 2 km altitude to exclude too-shallow clouds and observations near the installed site (Uma and Sama 2024).

2.3. INSAT-3D satellite-based Cloud Top Temperature (CTT)

To characterize the climatology of cloud tops during the observation periods, we also used data from the Indian National Satellite System 3D (INSAT-3D) based on a geostationary satellite over the study areas. We used cloud top temperature (CTTs data over the study periods at a spatial resolution of 4 km × 4 km (Mosdac.gov.in). INSAT is a Meteorological Geostationary satellite launched by ISRO (Indian Space Research Organization) on 26.07.13 with multiple payloads, namely (i) six-channel imager, (ii) nineteen-channel sounder, (iii) Data Relay Transponder (DRT), and (iv) Satellite Aided Search and Rescue(S&SR) System (Mosdac.gov.in). A smaller value of CTTs corresponds to deeper clouds, whereas higher CTTs correspond to shallower clouds.

2.4. Reanalysis data

A radiosonde is the best way to measure several environmental variables across different atmospheric pressure levels, as described below. All the variables are retrieved spatially at 0.25^{o} x 0.25^{o} grid resolution, and the temporal resolution is 1 day. We collected data from ECMWF (Hersbach et al. 2023) for 2024, covering March to September.

b1. CAPE: In the present study, we used the convective available potential energy (CAPE), which is crucial for storm development. CAPE is defined as the positive buoyancy of the rising undiluted parcel relative to its environment (Uma and Sama 2024)

$$\mathrm{CAPE} = \int_{\mathrm{LNB}}^{\mathrm{LFC}} (\mathrm{Tvp} - \mathrm{Tve}) R d d \ln \mathrm{P}$$

where Tvp and Tve are the virtual temperatures of the parcel and the environment, respectively. LFC is the level of free convection, and LNB is the level of neutral buoyancy, respectively.

b2. K-index and Total Totals index: K-index (KI) is an important thermodynamic index (George 2014; Grieser 2012) in meteorology, along with the total totals index (TTI) (Miller 1967), used to

assess atmospheric instability. These indices are derived from temperature and moisture values at various pressure levels and are directly related to temperature and moisture content at corresponding atmospheric levels (Grieser 2012). They are presented below.

$$KI = (Te850 - Te500) + Td850 - (Te700 - Td700)$$

where the temperature at 850 hPa, 700 hPa, and 500 hPa pressure levels are expressed as T850, T700, and T500, and the dew-point temperature at 850 hPa and 700 hPa pressure levels are represented as Td850 and Td700. The TTI is obtained from the differencing of the temperature and dew point temperatures at 850 and 500 hPa pressure levels (Miller 1967) and is stated below:

$$TTI = T850 + Td850 - 2T500$$

b3. Atmospheric dynamical conditions:

We also used the variables, namely, specific humidity (q in g-kg^{-1}), u (zonal) and v (meridional) wind components from 850 to 150 hPa to calculate the moisture flux (=q.v); where v is the resultant wind at each grid point, calculated from the zonal and meridional components of wind. We also used relative humidity (RH in %) and Omega (Pa-s^{-1}; vertical velocity(w)) data at 550 and 850 hPa. The lower-and mid-level tropospheric values can explain the roles of moisture and vertical velocity in determining the vertical reach of precipitating hydrometeors across different months (Liu and Zipser 2013; Kumar 2023; 2024). A negative value of Omega corresponds to updraft, whereas a positive Omega corresponds to downdraft, and the balance between RH and w can explain changes in precipitation characteristics (Liu and Zipser 2013).

We considered only 2024 to investigate the storm's vertical activity. Rainfall in 2024 over Kerala was normal, with a -19 to 19% deviation from the long-term period (Supplementary Fig. 1; India Meteorological Department report). Supplementary Figure 1 shows the time series of percentage departure of area-weighted seasonal and annual rainfall over the country as a whole. In 2024, annual rainfall over the country as a whole was 104% of its long-term average. Season-wise, rainfall across the country during the pre-monsoon (March to May) was 97% of the long-term average, whereas during the Monsoon (June to September) it was 108% of the long-term average.

3. Results

3.1. INSAT-based CTT climatology from pre-monsoon to monsoon months during 2024

Before analyzing the C-band-based Ze data, we presented the INSAT-3D-based monthly climatology of CTT from the pre-monsoon to the monsoon months (March to September, 2024) over the study areas. Figure 3a shows the frequency distribution of CTT between 180 and 200-K (a proxy for deep convection; Gambheer and Bhat 2000; 2001; Kumar 2025a). Figure 3b shows the frequency distribution of CTT between 200-240K, which is part of the rainy and non-rainy areas (Phadtare and Bhat 2020). The deepest convection (CTT<195-K) is more frequent during April to June. March has the least fraction of deepest CTT and a higher fraction of shallower CTT (Fig. 3). CTTs also show that pre-monsoon months have a higher fraction of deeper cloud tops compared

to other monsoon months, followed by August months, and are observed earlier in satellite-based observations (Fig. 3b; Romatschke and Houze 2011a;b) too.

Figures 4 and 5 show the spatial average of the CTTs during different months for CTT<220-K and 220-K<CTT<250-K, respectively. The 220-K represents deep convection (Gambheer and Bhat 2000; 2001) and will show the preferred regions and months associated with it. The INSAT-based spatial average of CTTs shows that April, May, and June have more pronounced deep convection (CTT<200K) than other months, peaking again in August and September, though with limited spatial extent (CTT<205-K). Regionally, the spatial locations of deep convection varied across months in 2024, and monthly differences reveal the land-ocean and coastal boundary contrast. For example, March shows the deepest convection only along the coastal boundary, whereas during April it extends across all study regions. June has the deepest convection over land-dominated areas, and then it decays or is absent during the July months, with a higher probability of shallower clouds. During August and September, the deepest convection (CTT<210-K) is mostly along the coastal boundaries. The Arabian Sea has much higher deep convection during the month of April, whereas the Bay of Bengal has higher deep convection during the monsoon season. These patterns are partially associated with the moisture flux flows and wind patterns (Joseph and Sijikumar 2004).

3.2. Storm Characteristics for pre-monsoon months to monsoon months for year 2024

Figure 6 shows (top row) the geographical locations (GLs) of storms in each 0.1^{o} x 0.1^{o} grid box from pre-monsoon to monsoon (March-September) season for the year 2024 and broadly shows the similar features observed earlier, especially during the monsoon seasons (Subrahmanyam and Kumar 2023; Uma and Sama 2025). The GLs from March to September reveal differences in the formation mechanisms of storms over land, over the ocean,, and near the coastal boundary. The maximum frequency of storms is observed in monsoon onset months, e.g., May and June, and storms are equally distributed over land and oceans. After June, spatial distribution changes, and storms are now mostly observed over the inland regimes of the study areas and are associated with monsoonal cloud characteristics (Kumar 2023; Uma and Sama 2025). In March, the storms are observed north of Thumba and are then evenly distributed over land and oceanic areas. Storms are equally distributed over ocean and land during May and June, but the storms penetrate more inland during May, and are observed earlier using the TRMM PR based statistics (Romatschle and Houze 2011a;b). During March and April, the storms are closer to the coastal boundaries. In July, August, and September, the higher frequency of storms is mostly observed over land, and storms penetrate further inland towards the east in WGs. These monthly variations in storm frequency from the ocean, along the coastal boundary, and in inland areas of India are associated with flow patterns during the pre-monsoon and monsoon seasons. The GLs of the storms are higher at the north-east side of the radar compared to the south-west of the radar observation area.

The second and third rows correspond to the storm's area (horizontal extension in km2 irrespective of their shapes) and ETHs (in km). Storm ETHs show higher land-ocean contrast than

storm area, e.g., horizontal extension (Uma and Sama 2024). Figure 6 also shows a higher frequency of larger-sized storms over the northern latitudes compared to the southern latitudes within the radar observation range, as well as on the east side of the WG during the monsoon onset month to monsoon season (May-September). The maximum ETHs are observed at the north of the radar observation range, along with the land-dominated regions in May-August months. March and September have the fewest ETHs (Subrahmanyam and Kumar 2023), with peaks in May and June, after which ETHs begin to decline toward lower levels. Land-ocean differences are more pronounced during the monsoon onset months (May and June), when deeper clouds are observed over land and topographic regimes than in other months. The role of the orographic features is also evident here, and storm ETHs are higher at the windward side of the WGs compared to the leeward side of the WGs. It is also observed that monsoonal storms are larger (horizontal extension) compared to pre-monsoonal storms, but they are shallower (fewer ETHs) compared to pre-monsoonal storms (Romatschke and Houze 2011a;b). The largest storms are observed in May, followed by July to August, whereas the smallest storms occur in March and April. The larger, deeper storm development indicates the blocking effect induced by the WGs around the radar site on storm organization (Uma and Sama 2025). Earlier studies have reported that LLJ plays a vital role in triggering intense convection and precipitation formation over the study regions (e.g., Gray and Jacobson, 1977; Jiang et al., 2007; Subrahmanyam and Kumar, 2022, 2023) during the monsoon seasons. The ETHs of the storms does not show a specific hotspot of locations during the monsoon seasons; however, land-dominated areas have a higher fraction of deeper storms during pre-monsoon months (Mar-May; highest in March), and this fraction peaks again in September. It shows that higher frequencies of storms with larger horizontal extensions) are observed at the windward side of the WGs compared to the coastal boundaries. However, the differences in the ETHs clearly show the land-ocean contrast from the onset month of the monsoon through the monsoon months (since March). Previously, using the X-band radar over the Northern-WGs (Mandhardev (18.04^{o}N, 73.85^{o}E)), Utsav et al. (2017) showed an increase in frequency of the storms on windward mountains associated with the orographic lift from southwesterly flow during the monsoon seasons, and observed here too. For example, we also observed an increase in storm frequency on the windward side of WGs during the monsoon months and along coastal boundaries.

Figure 7 shows the contoured frequency-by-altitude diagram (CFAD) for storms observed across various months, along with the average profiles. The CFAD provides the horizontal width/spectrum of Ze at different altitudes and reveals the intensity of the rain rate ($RR=a.Ze^{b}$) across different months (Yutur and Houze 1995). The CFAD reveals the differences between the pre- and post-monsoon months. Overall, in the pre-monsoon months, storms have greater variability in rainfall intensity, and rainfall is higher and more vertically extended than in the monsoon months. Storms during March are more organized, and the lowest probability of Ze (e.g., RR) is observed at higher altitudes, whereas the maximum probability of Ze occurs between 35 and 45 dBZ at altitudes of 3 to 5 km. As the pre-monsoon season progresses, a higher, more vertically extended, and more spatially spread CFAD is observed during April (>11 km) and May (>12 km). It is known that pre-monsoon months are more convective in nature (Romatschle and Houze 2011; Homeyer and

Kumjian 2015), and both months have higher Ze>38 dBZ at higher altitudes (up to ~5 km). March has the highest vertically extended CFAD among all the months. Once the monsoon season starts, less intense but well-organized CFADs are observed during June and July, and Ze>30 dBZ is well captured below the freezing altitude and is associated with more stratiform precipitation (Kumar and Bhat 2019). Romatschke and Houze (2011a;b) and Kumar (2016) observed that the mean reflectivity of 40 dBZ ETHs reaches up to 6 km in deeper convective systems during monsoon seasons using satellite-based observations, and is well captured in the peak monsoon months. Subrahmanmyam and Kumar (2023) used C-band radar during ISM and showed that a higher probability of 40 dBZ was observed at an altitude of ~4 km. The CFAD during August and September is weakest, revealing the absence of the monsoon season. Considering 40 dBZ as the threshold for intense storm activity, the 40 dBZ CFAD occurs at higher altitudes during pre-monsoon months and indicates more intense storm activity than during monsoon months. Spatially, pre-monsoon months have higher Ze compared to monsoon months. The differences in the spatial spread and vertical extent of reflectivity are associated with thermodynamic and dynamical conditions (Uma and Sama 2025) and are discussed later.

Figure 8 shows the average and median vertical profiles of Storm_VP observed during the different months (March-September). In the average vertical profiles, only altitudes are plotted where at least 90% of the profiles contribute to the Ze between 5 and 60 dBZ, to exclude less frequent observations from our study and make the results more significant. Throughout the months, the maximum Ze is observed somewhat above the surface (~2-3 km altitude) and then gradually decreases with height above ~3 km altitude; however, the rate of decrease in Ze is not uniform across all months. Similar features are also observed using the ground-based radar in northwestern India, and average profiles peak between 2-3 km altitude and then decrease (Subrahmanmyam and Kumar, 2018; 2021). It is observed that March and April have the strongest vertical storm cells, whereas September has the weakest storm cells and the lowest frequency. This is consistent with a previous study indicating that pre-monsoon months are more intense than monsoon months (Romatschke and Houze 2011a; Sindhu and Bhat 2021). The differences in the absolute Ze values are significant, and fewer vertical profiles contribute to higher altitudes than to lower altitudes. The rapid decrease in the Ze above 0°C in the middle and upper troposphere does not correspond to lower storm ETHs but rather to a very deep layer of smaller reflectivity values e.g. weaker storm activity (see the lower Ze values in CFAD; Lutz and Zipser 1994).

The average vertical profiles provide crucial information on storm intensity, storm-ETHs, and the relationship between rainfall intensity and storm-ETHs during the pre-monsoon to monsoon months. For example, a maximum height of 20 dBZ can be considered as a proxy for storm activity (Wu et al. 2018; Kumar 2017). Based on the average vertical profiles, the most frequent 20 dBZ radar occurrences are observed at altitudes of 7–12 km, depending on the month. In all the average vertical profiles, the radar bright band is absent due to intense updrafts and downdrafts (Lutz and Zipser 1994) and has been observed earlier over other land and topographic regimes of South Asia (Sindhu and Bhat 2018; 2021) using ground-based observations. The average vertical

profiles indicate how intense the storms are across the given altitudes during the different months. For example, March and April have deeper and more intense storms compared to other months, and the precipitation during the pre-monsoon months seems to be more convective in nature (Romatscheke and Houze 2011a;b). As the monsoon progresses, convective activity decreases, and most of the rainfall is contributed by stratiform precipitation, as seen in vertical profiles (Sindhu and Bhat 2019; 2021). September and August have the weakest storm activity at all altitudes.

The Ze values are not identical in the average and median vertical profiles; they show similar trends, e.g., a shape and a rapid decrease in Ze just above the freezing level, with a deep layer of lower Ze throughout the upper atmosphere. But the major differences are observed in their ETHs from the pre-monsoon month to the monsoon end month, and reveal the progression of storm activity during pre-monsoon to monsoon months (Fig. 8). We can also interpret these vertical profiles as evidence for near-complete glaciated zones and absence of the larger-sized particles/hydrometeors in the upper troposphere during different months. One important feature is vertical velocity, which determines the vertical reach of hydrometeors in the upper troposphere; a low vertical velocity is insufficient to lift raindrops above the freezing level (Heymsfield et al. 2010). To estimate vertical velocity, we used the Omega (pressure-vertical velocity) at 500 hPa, as discussed later.

3.3. Individual rain hotspots characteristic of embedded within the storms (IIVP_storm)

Figure 9 shows the GLs of individual IIVP_storm (Ze>35 dBZ), and the spatial differences between the pre-monsoon and monsoon months are higher here than in the VP_storm GLs. For example, a higher fraction of IIVP_storm is observed during the pre-monsoon seasons compared to monsoon seasons (Romatschke and Houze 2011a;b). Spatial differences such as land-ocean contrast and differences over the AS, IEO, and BOB are higher during monsoon months than during pre-monsoon months and are associated with monsoonal synoptic conditions and a higher fraction of stratiform precipitation (Romatschke and Jouze 2011a, b; Kumar 2016; Dash et al. 2018). A remarkable difference is observed among the three oceanic areas: AS, BOB, and IEO. IEO has a much higher frequency of IIVP_storm compared to AS and BOB during the pre-monsoon season. Pre-monsoon months show fewer differences than monsoon seasons between land and oceanic regimes. Both land- and ocean-dominated areas have a higher fraction of IIVP_storm during March and April, and in May and June, it is mostly concentrated near the coastal boundaries. August and September have the lowest fraction (occurrences) of IIVP_storm . The differences in the GLs of IIVP_storm and VP_storm show that during the pre-monsoon months,, cloud systems exhibit a higher frequency of individual intense precipitation hotspots than during the monsoon months. In other words, within the cloud systems, there is a higher probability of intense precipitation spells compared to monsoon months. The fewer IIVP_storm over the AS and closer to the coastal boundary during the monsoon seasons are associated with the moisture transported from the AS to land and topographic regimes. Table-1 shows the number of IIVP_storm used in the present study at different horizontal extensions.

Figure 10 shows the average vertical profiles of IIVP_storm at different horizontal scales (e.g., 9, 25, and 49 km^2). Again, when calculating the average Ze, altitudes with sample sizes less than 10% of the maximum across all altitude levels are omitted to make the profiles more significant. All three cases show similar vertical trends in Ze but have different ETHs and lower Ze values. These average vertical profiles can be grouped into three categories. First, March and April, which have the most intense vertical convective cells, are followed by May and June. The strongest Ze profiles in March and April may be associated with a higher frequency of Ze>35 dBZ over land-dominated areas than over oceanic areas (Fig. 9; Perterson and Rutledge 2001; Xu and Zipser 2012; Bhat and Kumar 2015). The weakest convective cells can be grouped in July-September, that is, during the withdrawal of the monsoon season, and stratiform precipitation mostly dominates near the study regimes. The pre-monsoon months have more intense IIVP_storm profiles than the monsoon months and are observed earlier in TRMM-based observations (Romatschke and Houze 2011a,b). The monthly differences in rainfall intensity are higher in the mixed-phase altitude and glaciated zones than in the lower troposphere, and are observed earlier in TRMM- and GPM-based observations across the globe (Kumar and Silval 2019; 2020). All the IIVP_storm vertical profiles at different horizontal scales show similar trends; however, the maximum altitude at which the average Ze is observed varies. For example, July to September have the least intense IIVP_storm profiles, but they are deeper than in May and June. June has the least IIVP_storm tops, followed by July. The ETHs vary across different horizontal scales; for example, it is lowest in a small horizontal grid box (3 km x 3 km). This reveals how quickly rainfall intensity increases horizontally compared to larger grid boxes, where there may be intrusion of other intense IIVP_storms or tilting of intense convective cells. The differences in the maximum heights of average profiles are highest in March and April among different grid boxes, ranging from 9 to 25 and 49 km^2, whereas the least differences are observed in June and July. IIt also shows that IIVP_storm is more vertically developed/extended during the pre-monsoon months than during the monsoon months, and that the tilting of precipitation tops is greater at higher altitudes. The intensity remains the same across all horizontal extensions compared to ETHs. Again, based on the maximum altitude of 20 dBZ, storm activity is most pronounced in March and April, with the greatest horizontal extent, whereas the least activity is observed in July. Figure 10d shows the ETHs (maximum height of 5 dBZ). When we consider the 5 km x 5 km grid box (25 Km^2). April has the highest ETHs (>12km) followed by August and September. The fewer differences below 3 km altitude reveal similar rainfall intensity between the pre-monsoon and monsoon months. The deep convection (ETHs>10 km; Houze et al. 2007; Kumar et al. 2019b) is highest during the March and April months, whereas the least deep convection is observed during the June and July months, and corresponds to more stratiform precipitation during the monsoon seasons.

To investigate the impact of the horizontal scales on the vertical reach of IIVP_storm, we plotted the differences in IIVP_storms. Figure 11 shows the difference in the number of IIVP_storm reaching different ETHs at different horizontal scales. The maximum differences are observed at ETHs below the 6 km altitude and that too in May and June months. The opposite trends are observed below and above the 4 km altitudes. Above the mixed-phase altitudes, different trends are observed and pre-monsoon months have more differences in the IIVP_storm, which are

crossing above the 9 km^2 altitudes. It shows that ETHs decrease rapidly in May and June as the horizontal extension increases; e.g, there is a higher chance in IIVP_storm extended vertically at the least horizontal and medium horizontal extensions. It also showed that tilting is lower during the mentioned months than in other monsoon months. May and June have higher frequencies of shallower ETHs at higher horizontal scales. March and April have higher numbers of IIVP_storm with the least ETHs at the highest horizontal extensions. As the horizontal extension increases (>9 km), the number of IIVP_storm decreases from small to mid horizontal extension and from mid to highest horizontal extension, and this is observed in April and May. It also reveals that vertical extension above 9 km is highest at lower horizontal extension in April and May and least in the monsoon months. In other words, it shows that during the monsoon months, IIVP_storm can be vertically extended with greater horizontal extension, and the tilting of the precipitation tops is higher at lower horizontal extension in April and May.

Figure 12 shows the CFAD of IIVP_storm across three horizontal grid boxes and again highlights differences in the vertical extent and spread of Ze width across grid boxes and months. The vertical extension of Ze across different months and horizontal grid boxes is not identical. The maxima in Ze (red color) show different vertical extensions for the least horizontal grid boxes, and the highest vertical extension is observed in April (Ze>35 dBZ extends beyond 6 km altitude; Ze>20 dBZ extends beyond 12 km altitude). At higher grid boxes, the maximum Ze is more horizontally spread, but overall, there is little difference in their vertical extent. The Ze decreases more rapidly above the freezing level for higher horizontal grid boxes, especially during pre-monsoon seasons. It shows that pre-monsoon months' precipitation ETHs are dominated by higher Ze than in monsoon months, where rapid precipitation under higher moisture content leaves fewer hydrometeors reaching higher altitudes (Liu and Zipser 2013). Pre-monsoon months have a greater spatial extent of Ze than monsoon months. The tilting of CFAD or reduction of Ze is more pronounced in Monsoon months compared to pre-monsoon months. The role of horizontal grid boxes is clearly visible here, revealing that the rate of decrease in Ze depends on the selected grid boxes, with the lowest in the middle row (25 km^2).

3.4. Characteristic of intense vertical profiles

Figure 13a and 13b show the average vertical profiles of the IVP8s and IVP3s during different months, whereas Figure 13c and Figure 13d show the frequency distribution of ETHs of IVP8 and IVP3s used in the present study. The vertical profiles can be distinguished into two layers: below and above the 4 km altitude (IVP8) and the 3 km altitude (IVP3), where Ze increases with decreasing altitude, and Ze decreases with increasing altitude, respectively. The higher differences are observed in IVP8s than in IVP3s, the opposite of satellite-based observations (Bhat and Kumar 2015; Kumar and Bhat 2016). This could be because of the minimum observable differences in Ze, both ground- and satellite-based radar, which are much higher for TRMM and GPM (~17 dBZ) than for C-band radar (~5 dBZ). Again, March and April have the most intense convective cells compared to other months; the differences are smaller than in storm-based vertical profiles. The major differences are observed in the inversion layer, where the Ze starts decreasing with height, and these changes occur as the pre-monsoon-to-monsoon transition progresses. IVP8s show the

higher monthly differences compared to IVP3s, and the major monthly differences are observed above the freezing altitudes. IVP3s show a similar structure to the storms shown, but IVP8s show completely different features compared to other vertical profiles. It reveals that not only the Ze threshold but also the height thresholds play a vital role in monthly variations in rainfall intensity, similar to satellite-based observations (Kumar et al. 2024b). The regional differences are lower below the freezing altitude (~5 km) and increase at mixed-phase altitudes and in the upper troposphere, e.g., in glaciated zones. In March and April, vertical cloud cells are most intense, followed by May and June, similar to earlier observations.

The ETHs of IVPs show fewer differences across months; however, in a small difference, the June (September) month has the highest fraction of the lowest (higher ETHs above 10 km) ETHs for IVP3s and IVP8s, respectively. The inversion layer for IVP8s and IVP3s is around 9.5 km and 6 km, respectively. IVP3s show the largest differences in warm rain (below 5.5 km altitude), and above that altitude, differences are very small across months. However, IVP8s show different trends. Here, the differences are smaller in the mixed-phase altitudes (~9.5 km). The higher ETHs in the average profiles are observed in August and September. It shows that once the IVP8s cross the mixed phase, they are more likely to reach deeper, which leads to larger monthly differences.

One of the most important observations, based on horizontal scales, is that monthly storm intensity changes across all three types of vertical storms depend on the Ze and height threshold used here. For example, June has much less storm activity in Storm_VP than May, and we can consider June a weaker storm-activity month at higher horizontal extension. However, in IIVP_storm and IVPs, May and June have comparable intensities, revealing that as horizontal extension increases, vertical storm activity matches in May and June. Similarly, July has the weakest Ze profiles in IIVP_storm and IVPs (less horizontal extension), whereas September has the weakest vertical profiles during Storm_VP (higher horizontal extension). This shows that, within a few months, intense storm activity can develop at small scales with convective intensity similar to other months, where intense storm activity develops only at large horizontal scales. We must consider these findings in numerical models to predict storm activity. Minute differences in Ze (∼1 dBZ) are observed in IIVP_storm and IVPs below 4 km altitude from the pre-monsoon to the monsoon months. This is linked to similarly intense near-surface convective activity. This shows that large-scale storms show larger differences below 4 km altitude than smaller-scale storm activity.

4. Discussions

In average vertical profiles, a higher Ze in the middle and upper troposphere can serve as a proxy for intense convection and higher updraft speed (Zipser et al. 2006). Here, we did not discriminate between land- and ocean-based cloud cells; the spatial distribution of storms shows that land- and topographic-regime storms are more intense than those in the ocean. This has been reported previously (Pen and Rutledge, 2001; Zipser et al., 2006). The differences in the average vertical profiles highlight the importance of the reference height, Ze thresholds, and the horizontal grid used to define the storm cells, as observed previously (Kumar 2023). The variation in all the

average vertical profiles can be viewed in two ways: first, it decreases with increasing altitude; second, for the cloud/precipitation tops, it decreases towards the surface. Both features result from the different cloud micro-physical phenomena (Heymsfield et al. 2010). This can be explained as follows: in the first scenario, under weaker updrafts, hydrometeors had more time to grow and become heavy through ice physics, and thus fell more quickly (Heymsfield et al. 2010). In a different view, a stronger updraft does not provide sufficient time for ice microphysics to produce larger hydrometeors in mixed-phase regimes, which could take condensed water at higher altitudes. These hydrometeors can grow in size in the upper troposphere, and larger particles begin to fall from the cloud tops with higher terminal velocity when their terminal velocity exceeds the updraft speed, mostly during the mature and dissipating phases. While falling within the clouds, the hydrometeors can grow in size by deposition, accretion, and aggregation. Since Ze varies with the 6th power of hydrometeor size, it increases as hydrometeors approach the surface. Below the freezing altitudes, it depends on the types of profiles we selected. For example, considering the storms as individual cases shows no inversion layer, and Ze only increases towards the surface; this tendency is more common in convective rainfall events (Kumar 2024). This shows that, overall, in storms, the rain rate tends to increase towards the surface only at large (horizontal) scales. However, when we consider smaller horizontal scales, the average Ze tends to decrease towards the surface below the freezing altitude observed in earlier reports (Kumar 2016). This could also be associated with the strong attenuation in the heavy rainfall events (Kummerrow et al. 1998; Hirose and Nakamura 2002). This tendency is weakest at the end of the monsoon months, when the monsoon's withdrawal reduces convective rainfall.

It is well known that background atmospheric stability, atmospheric conditions such as moisture, and dynamical characteristics in the lower to mid-troposphere are responsible for storm severity. In the past, it has been reported that the CAPE, K-index, and TTI indices can serve as proxies for atmospheric instability that drives storm development (Louf et al. 2019). Since the spatial and temporal resolutions of the two datasets do not match, we will discuss the possible relationship in the distributions basis only. Jha et al. (2021) reported that the intensity of mid-tropospheric humidity, instability (CAPE and CIN), and dynamical indices determine storm characteristics. However, no strong correlations or direct connections are observed between the thermodynamic indices and storm intensity (Louf et al. 2019; McTaggart-Cowan et al. 2020; Jha et al. 2021; Uma and Sama 2024). They observed that higher CAPE and indices are associated with smaller & deeper storms, and even a lower-to-moderate CAPE with other indices can generate severe storms (Jha et al. 2021; Sindhu and Bhat, 2019). In a recent study, Uma and Sama (2025) also reported that even a smaller CAPE over the AS can produce severe storms compared to BOB during the monsoon seasons. Figure 14 shows the cumulative frequency (upper row, a:CAPE, b:K-index, c:Total totals Index) and frequency (bottom row, d:CAPE, e:K-index, f:Total totals index) distribution of the mentioned variables. CAPE shows larger monthly differences than other indices. Overall, monsoon periods have less CAPE compared to pre-monsoon months and are responsible for less intense convection (Romatschke and Houze 2011a;b). It is observed that April and May have CAPE values exceeding 1500 kJ kg^{-1}, with March following. It also shows that months with higher CAPE correspond to weaker vertical profiles, whereas the months with the lowest monthly CAPE (August

and September) have the weakest vertical profiles. March has the lowest CAPE and also the lowest vertical extent and CFAD spread. So, in the monthly variation, we see a strong correlation between the CAPE and the intensity of vertical thunderstorm profiles. The other indices' values are at their lowest in March and April compared with other months, and there is no strong correlation between thunderstorm severity and the indices' magnitudes.

Figure 15 shows the cumulative distribution and boxplot of the environmental indices (CAPE and Indices). March and August have the lowest CAPE values, followed by September, and all CAPE values are below 2000 KJ-kg-1. The K-index shows different characteristics compared to CAPE, and March has a much higher fraction of low indices than the other months. KI >30 values indicate favorable conditions for storm formation, and these values increase from May onward. March has the lowest CAPE and index values, followed by September. The TTI index shows the least variation among the months. About 95% of the population from May to August has values greater than 30. At the same time, March has the lowest KI and TTI Index. April has a much lower KI index but a TTI index comparable to May through September. CAPE values are highest in April and May, followed by June and July. August has the lowest CAPE values. Index values are higher in May and, in general, higher in Monsoon months than in March and April. During the monsoon months, all CAPE values are below 2500 KJ-kg-1, whereas in April and May, the 5% change exceeds 3000 KJ-kg-1. These higher CAPE values also correspond to a higher frequency of IIVP_storm and the most intense Ze values across all vertical characteristics.

Higher CAPE in humid months supports frequent storm formation (in terms of numbers; May to July); however, even with a drier atmosphere and higher CAPE, lower indices in April produce frequent storm activity. In March and September, lower CAPE and a drier atmosphere limit frequent storm activity; monsoon months such as August and September are less humid. The larger CAPE values suggest a well-mixed elevated layer (2-4 km) and an unstable environment with strong convective updrafts. The KI provides evidence of storm-formation potential in both seasons, but predominantly in particular months.

However, the relationship between the CAPE and updraft speed is quite complex. Larger CAPE and index values can indicate convection and the formation of multiple storms across months. However, entrainment from the surrounding environment also reflect

The basic atmospheric conditions (e.g., temperature, humidity, and wind fields) are completely different during the pre-monsoon and monsoon seasons. The transported moisture flux plays a vital role in determining the storm's severity and its movement (Joseph and Sijikumar, 2004). The transition from the pre-monsoon to the monsoon over Kerala and AS is associated with increased diabatic heating, and latent heat release during precipitation enhances the cross-equatorial flow (Joseph and Sijikumar, 2004). The increase in wind speed stimulates higher moisture fluxes, and low-level jets are responsible for large-scale moisture transport (Joseph and Sijikumar, 2004). It is well known that the lower troposphere (<4 km) is relatively cooler and more humid than the remaining tropospheric levels during the monsoon seasons compared to pre-monsoon seasons (Sindhu and Bhat 2019; Parker et al. X) because of winds during the southwest monsoon season, which brings more moisture to the Indian land. Figure 16 shows the moisture flux (=q.*v*) for 6 to

11 latitudes at different pressure levels; q is specific humidity and *v* is the resultant wind speed obtained from the U and V components of the wind. This shows the role of the moisture buildup and its removal from pre-monsoon months to the monsoon months. The striking feature is the moistening of the lower boundary layer and mid-troposphere that occurs before the onset of the summer monsoon and is associated with increased wind speed due to the low-level jet. March and April have the least zonal variation of moisture fluxes, although April shows a sudden increase in moisture fluxes at 650 hPa compared to March, which has higher moisture fluxes only at lower altitudes (higher pressure levels). Monsoon months (June-July) have the highest moisture fluxes, which build up at higher altitudes (low-pressure levels) and are responsible for the greater horizontal extent and ETHs, but not the convective intensity of the storms. The moisture flux is highest in July, but it has the fewest ETHs and the lowest convective intensity. The opposite trends/relationships between moisture flux and rainfall intensity reveal microphysics-dominated processes under higher moisture content and RH (Liu and Zipser 2013; Kumar 2023; 2024). Under moist conditions, precipitation forms rapidly, and collision-coalescence processes are effective (forming larger raindrops), increasing hydrometeor size and causing them to fall quickly under gravity. It leaves fewer hydrometeors to go deeper into the atmosphere and is observed in Fig. 6-8 (Liu and Zipser 2013).

Vertical velocity (*w*), e.g., updrafts and downdrafts, also plays a vital role in storm development, and we used Omega values in Pa-s^{-1} at two pressure levels, namely 850-hPa and 550-hPa. The development and longevity of the storms depend on the balance between thermodynamic and dynamical processes. Liu and Zipser (2013) showed that vertical velocity (updraft/downdraft) plays a critical role in determining ETHs under different RH conditions (Kumar 2023; 2024). The humidity patterns in the lower to mid-troposphere are responsible for precipitation intensity. In a recent study, Kumar (2025a;b) shows that a dry mid-troposphere restricts the vertical growth of precipitation as well as their rainfall intensity during ISM seasons. Also, Davis et al. (2003) showed that a moist mid-troposphere favors intense storms during the Australian summer monsoon. Figure 17 shows the balance between the microphysical variable (relative humidity, RH) and the dynamical variable (vertical velocity) across different months during the study periods at 550 and 850 hPa. It is clearly observed that monsoon months have higher RH, e.g., June-September RH is always higher than 55-100% compared to pre-monsoon months, where RH lies between 10 to 90%. It is clearly observed May-August has the highest RH (more than 90% RH) at 550 hPa compared to remaining months, that too associated with the updraft (w<0.4 Pa-s^{-1}) and associated with the intense profiles (Fig. 6). March and September months have the less Ze and are associated with both weaker updraft and downdraft, and response to weaker intense profiles with less ETHs (Fig. 6). However, since August and September months have a more RH corresponding to downdraft, and may be associated with the higher Ze and a sudden peak in average profiles. However, it needs to be investigated in detail in the future. During the pre-monsoon months, March has the fewest updrafts and downdrafts with the lowest RH, followed by April, and peaks in March during the pre-monsoon season, as reflected in the storms' characteristics (Fig. 6;7).

Heymsfield et al. (2010) showed that even a small perturbation in mixed-phase altitude strongly affects the vertical gradient in Ze. The Ze trends within mixed-phase altitudes among different profile types, defined by different Ze and height thresholds, are determined by updraft speed and hydrometeor outflow in the mixed-phase altitudes. This balance determines hydrometeor size within the mixed-phase altitude and, in turn, the Ze. For example, lower updraft speed gives hydrometeors more time to grow, and as they fall, they can reach a higher downdraft speed. Another scenario is that a stronger updraft could bring more condensed water to higher altitudes, while hydrometeors grow and fall out when large downdrafts dominate updrafts. Zipser and Lutz (1994) used the C-band radar at Darwin, Australia. They reported vertical Ze gradients between 5 and 9 km altitude, with values of 1.5 and 3.5 dBZ km-1 over mid-latitude continental and tropical continental storms. Compared with existing studies, the vertical Ze gradient in the present study ranges from 2.8 to 4.6 dBZ km-1 and is comparable with previous findings in land regions. For example, Bhat and Kumar (2015) studied the vertical gradient in intense convective profiles. They observed that the vertical Ze gradient lies between 3 and 3.5 dBZ km-1 over land-dominated regions during monsoon seasons. Toracinta et al. (2002) observed a vertical Ze gradient of 2 dBZ km-1 in convective storms over League City (USA) using the WSR-88D radar. These broad similarities in average profiles may limit understanding of larger differences in cloud microphysical processes. Monsoon months have higher slopes than pre-monsoon months (Fig. 18), and lower slopes for ICC8 and Storm_VP and deeper ETHs. The slopes for different storm types range from 2.8 to 4.6 dBZ-km-1 and are similar to those in previous studies. The higher slope in the mixed-phase altitude and the lower vertical extent in convective clouds suggest that hydrometeors increase in size while moving downward with weaker updrafts during the monsoon season. The opposite trend is observed with stronger updrafts, mostly over the pre-monsoon. In that scenario, the cloud air parcel spends less time in the mixed-phase altitude, so most condensed water can be carried to higher vertical levels. Thus, the slope is mostly governed by the growth of ice hydrometeors coming from the upper troposphere.

5. Conclusions:

The present study explores the vertical characteristics of storms at different horizontal scales and Ze thresholds in 2024, from the pre-monsoon to the post-monsoon months. The main aim of the present study is to document the vertical characteristics of storms during the pre-monsoon and monsoon seasons in 2024 at the monsoon-onset location in India. The collected ground observations, along with reanalysis data, provide insights into the differences in their nature and the plausible reasons behind them. The results presented here are based on Ze variation. The main conclusions from the present study are listed below:

1. The INSAT-based geostationary satellite shows the buildup of deep convection from the pre-monsoon months to the monsoon season. The deep convection is located along the western coastal boundary during March and penetrates inland areas in subsequent months. Land-ocean contrasts are more visible during the monsoon season compared to the pre-monsoon months.

2. C-band-based storms are larger (horizontal extension) in the north-east and topographic regimes of the study area, with deeper storms (higher ETHs) during the April to May months, whereas shallower storms (lower ETHs) are observed in March and September months. The deepest storms are observed during April and May. Monsoon onset months, e.g., May, have both larger and deeper storms compared to monsoon months, whereas they are as large as monsoon months (June-August), but shallower compared to the onset month.

3. Pre-monsoon months have more intense storms (stronger vertical profiles) compared to monsoonal storms. Pre-monsoon-based deeper cloud cells are isolated compared to monsoonal deeper cells, which are associated with the larger cloud systems.

4. June has much less storm activity in Storm_VP than May, and we can consider it a weaker storm-activity month at higher horizontal extension. However, in IIVP_storm and IVPs, May and June have comparable intensities, revealing that as horizontal extension increases, vertical storm activity matches between May and June. Similarly, July has the weakest Ze profiles in IIVP_storm and IVPs (less horizontal extension), whereas September has the weakest vertical profiles during Storm_VP (higher horizontal extension). This shows that within a few months, intense storm activity can develop at small scales with convective intensity similar to other months. In contrast, in other months, it can develop only at large horizontal scales.

5. Individual rainfall hotspots (IIVP_storm) show a higher frequency during pre-monsoon months than during monsoon months, indicating higher convective activity during the pre-monsoon months. August and September have the least frequency of IIVP_storm, e.g., intense rainfall hotspots. It shows that the numbers of IIVP_storm decreases rapidly in May and June months as the horizontal extension increases, e.g, there is a higher chance of IIVP_storm extending vertically at the least horizontal and medium horizontal extensions. Large-scale storms have higher differences below the 4 km altitude compared to smaller scale storm-activity.

6. The ETHs in the average vertical profiles of intense rainfall spots (IIVP_storm) depend on the spots' horizontal extent. Differences in ETHs across different horizontal scales are greater during the pre-monsoon months than during the monsoon months. During the monsoon months IIVP_storm can be vertically extended with higher horizontal extension, and, tilting of the ETHs is higher at higher altitude in April and May.

7. One of the most striking features is the buildup of moisture flux in the middle and upper troposphere from the pre-monsoon to the monsoon months. It is also observed that moderate CAPE can produce severe storms.

The present study explores differences in storm vertical structure between the pre-monsoon and monsoon months for the year 2024. These storms are associated with heavy rainfall and lightning, resulting in excess rainfall and damage to property and people's lives; thus, their nowcasting is important. The differences in the land-ocean contrast is higher in monsoon months, and pre-monsoon months are more convective in nature but with fewer occurrences. One of the major

differences observed here is that the monthly differences in the vertical structure depend on the thresholds (in Ze) and the horizontal extension used in the present study. A detailed investigation using multiple years and modeling of these observations will lead us to the next step: examining the role of storm dynamics and thermodynamic conditions across different seasons. Understanding the storm's vertical structure leads to better short-range weather forecasting and improved convective parametrization schemes. Our results advance knowledge of storm scales, with implications for short-range weather forecasting and the development of new convective parametrization schemes. The vertical characteristics of storms at different horizontal scales are relevant for remote sensing of precipitation, particularly because the footprint of space-based radars covers 90% of convective precipitation. Thus, from both scientific and practical points of view, storm vertical structure matters across their horizontal scales.

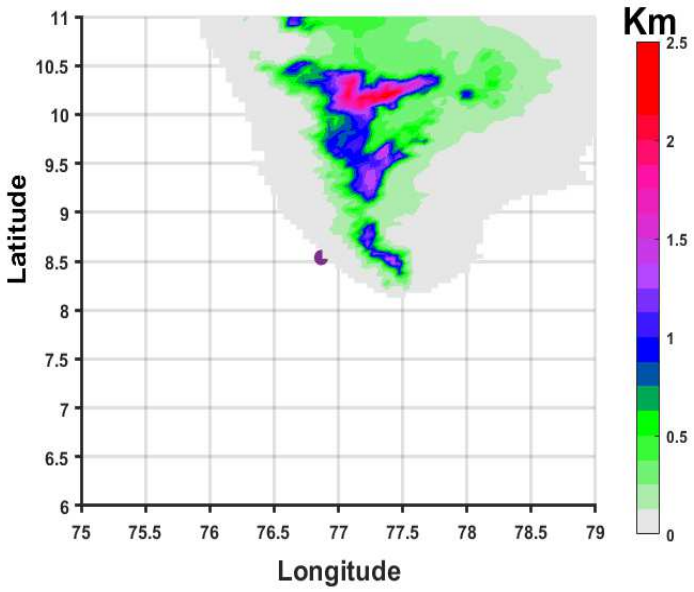

Figure 1. Geographical location of C-band DWR at THUMBA in brown dots (76.7^0E, 8.5^0N). The study regions also consist of the orographic features.

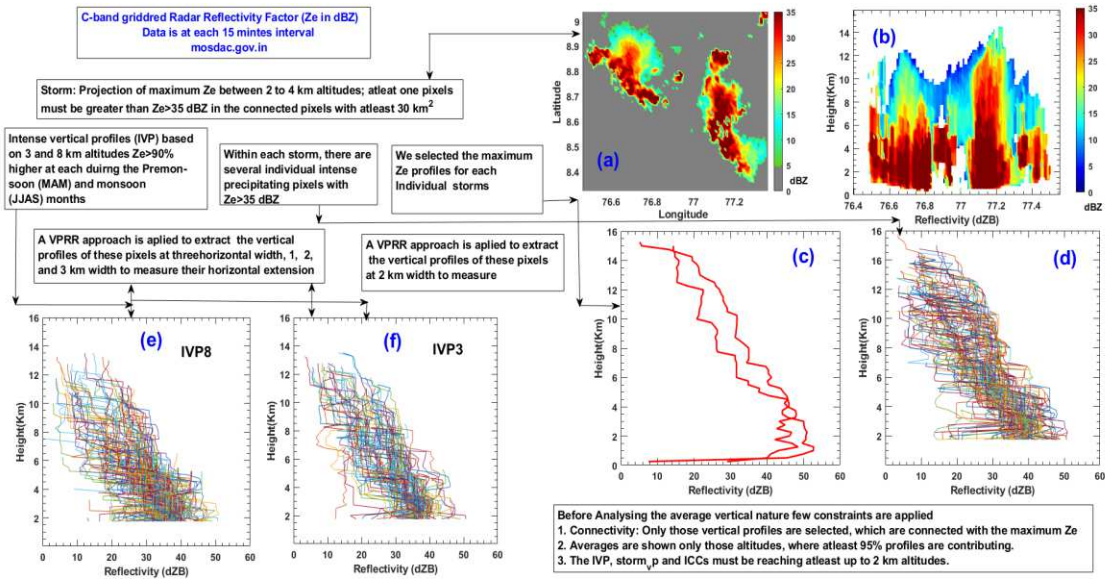

Figure 2. A flow diagram of the different vertical profiles used in the present study. (a) Storms selected in the present study: composite radar reflectivity factor at 2-4 km altitude for the C-band radar on 11 May 2024 at 11:55 PM. (b) Composite Ze for height-longitude abscissa. (c) Example of the Vertical profiles of VP_storm for two individual storms, (d) Example of the vertical profiles of the IIVP_storm (35 dBZ hotspots), (e) Example of vertical profiles of Intense vertical profiles based on 8 km height and Ze95 thresholds, (f) Example of vertical profiles of Intense vertical profiles based on 3 km height and Ze95 percentile thresholds.

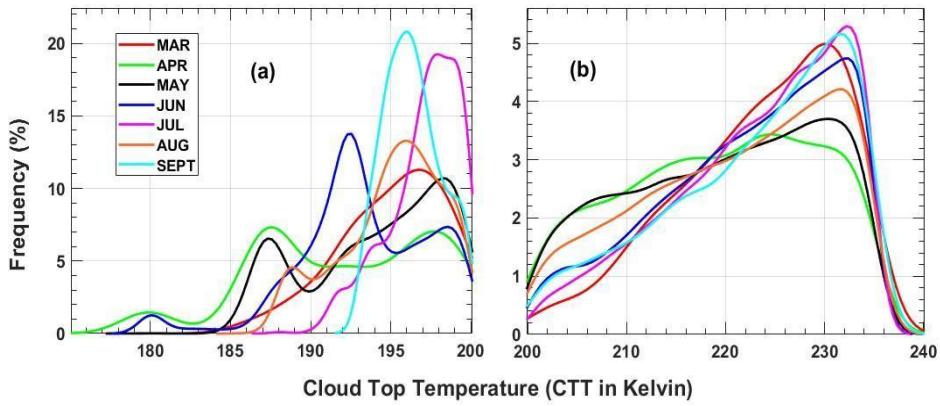

Figure 3. Frequency distribution of cloud top temperature (CTT) over the selected areas during the study periods. (a) CTT less than 220K; (b) CTT between 220 and 240-K. The CTTs are in Kelvin.

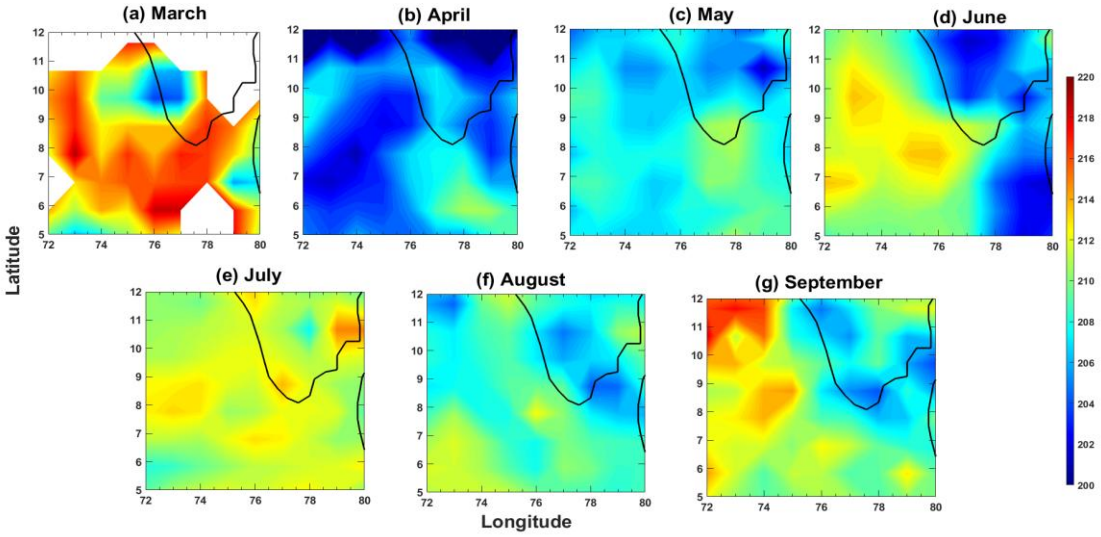

Figure 4. Monthly spatial climatology of the cloud top temperature (CTT) for the CTT less than 220K. The colorbar shows the CTT in kelvin.

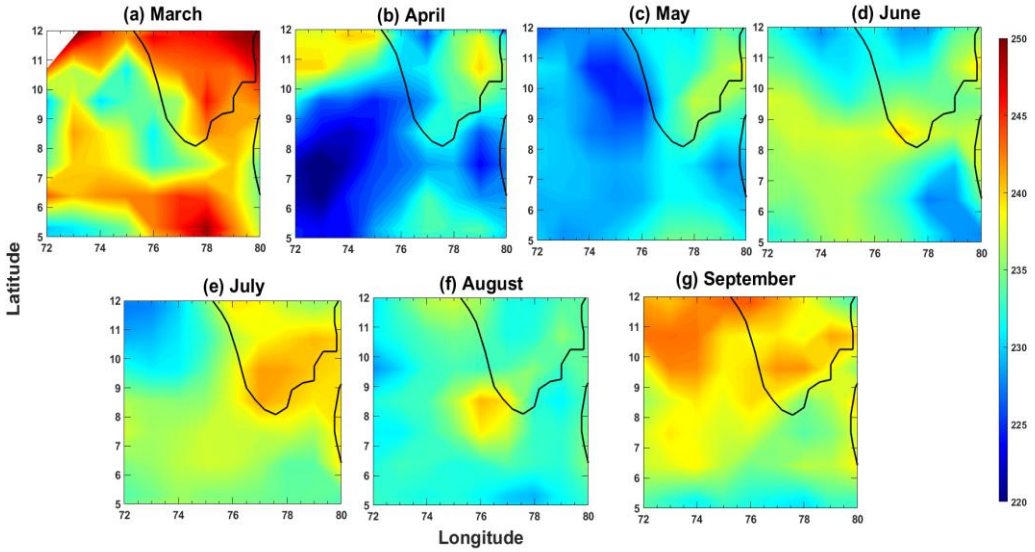

Figure 5. Monthly spatial climatology of the cloud top temperature (CTT) for the CTT higher than 220 K and less than 250K. The colorbar shows the CTT in kelvin.

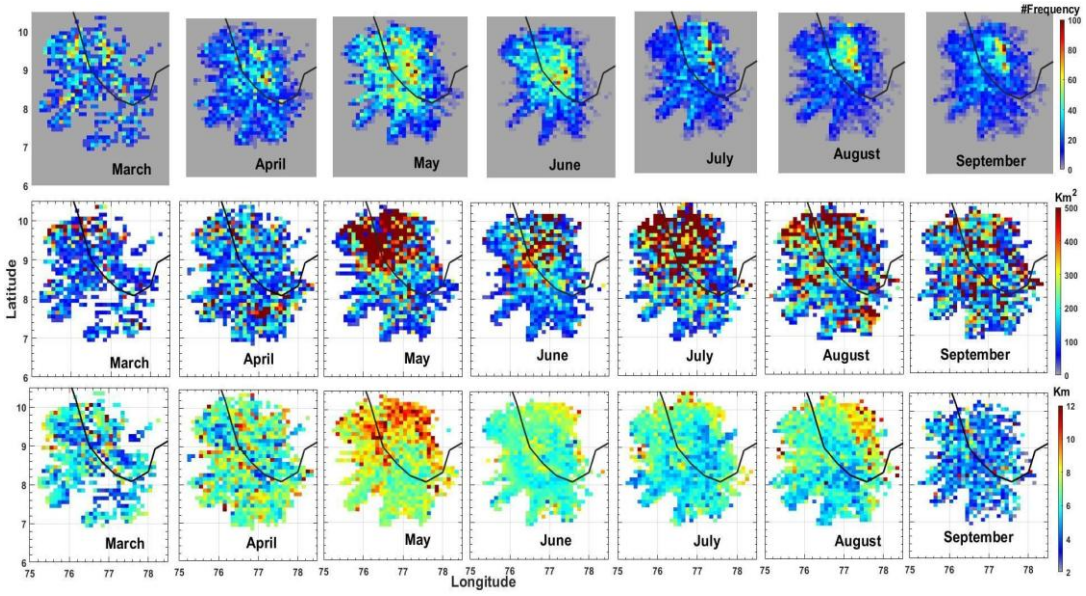

Figure 6. Monthly spatial characteristic/properties of storms used in the present study, (Top row) geographical location of the storm in each 0.1° x 0.1° grid boxes, (Mid row) Horizontal extension

of storms used in the present study in each 0.1° x 0.1° grid boxes in Km^2 (Bottom row) precipitation top altitude in the storms used in the present study in each 0.1° x 0.1° grid boxes in Km.

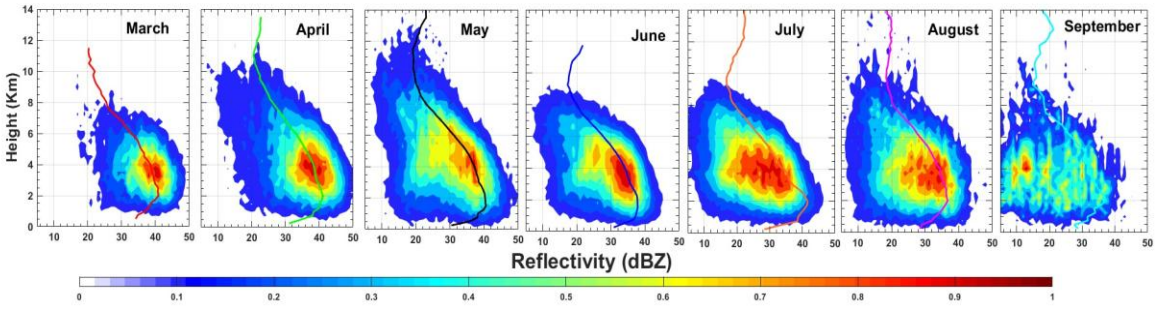

Figure 7. Contoured frequency by altitude diagram (CFAD) of storms used in the present study. The shaded regions represent the probability of Ze at the particular height. The colorbar is showing the relative occurrences of specific Ze at specific altitudes.

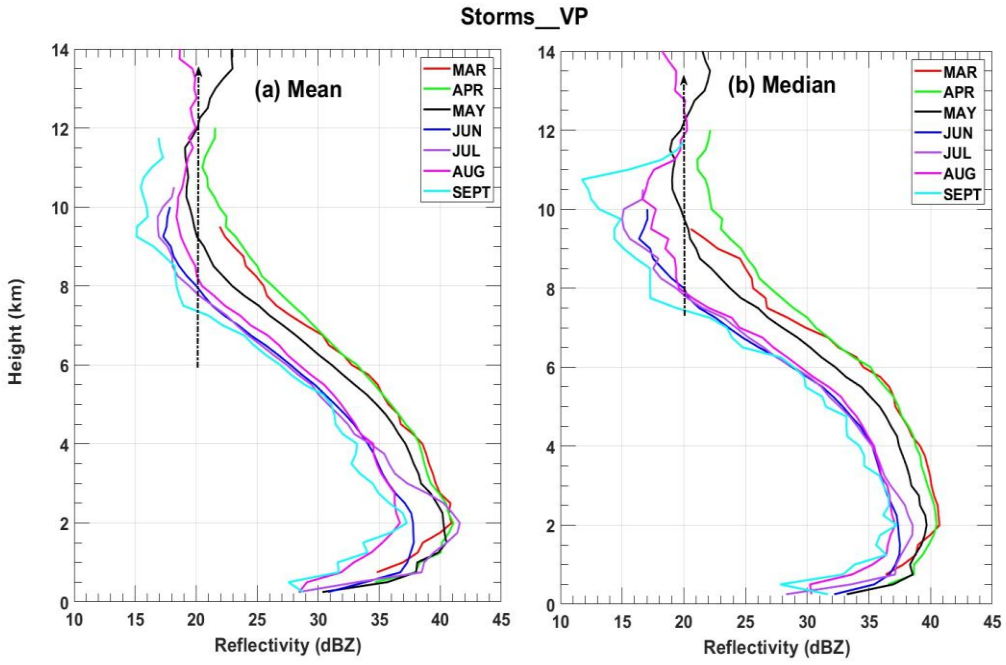

Figure 8: (a) Average vertical profiles of radar reflectivity value observed in storms_VP during different months, (b) Median vertical profiles of radar reflectivity value observed in storms_VP during different months used in the present study. The average and median profiles are shown

only at altitudes where at least 95% of profiles contribute. The vertical arrow is drawn at 35 and 20 dBZ to indicate convective activity, as the 20 dBZ altitude represents storm activity.

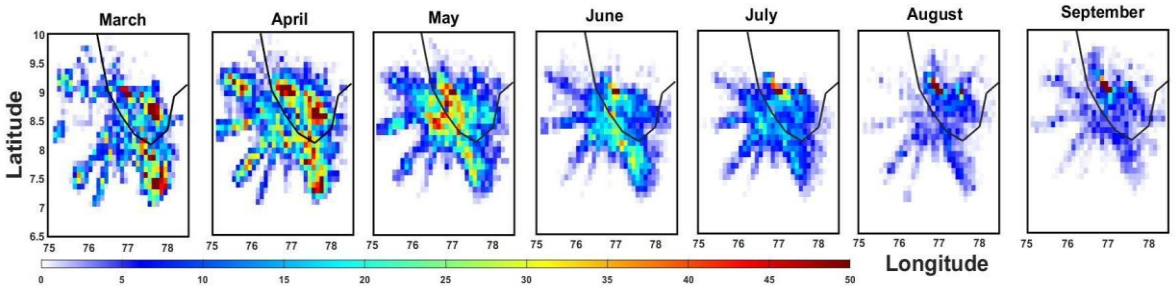

Figure 9: Spatial distribution of IIVP_storm (hotspots of 35 dBZ) over the selected areas during the study periods. The colorbar shows the relative probability of Ze occurrences at specific altitudes.

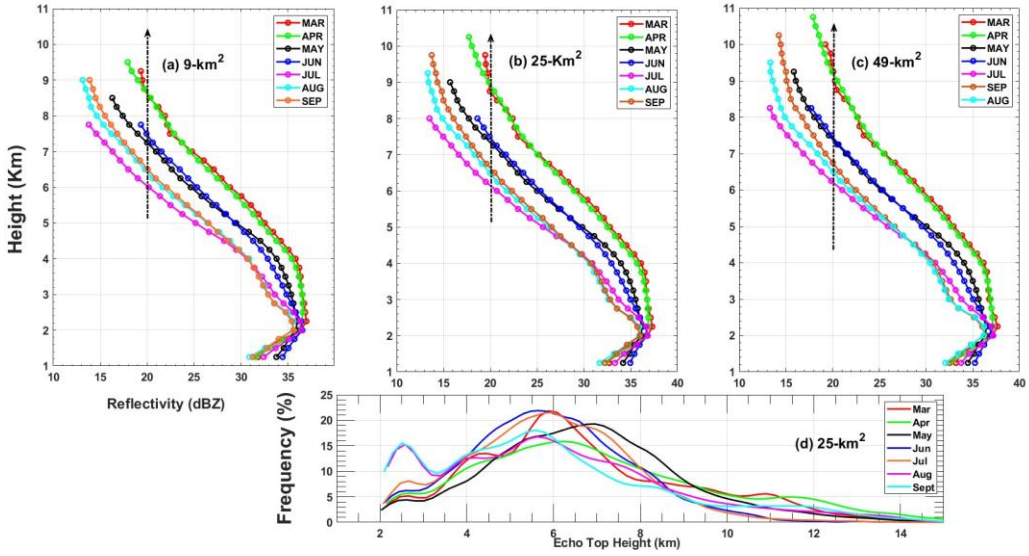

Figure 10. Average vertical profiles of IIVP_storm (a) average vertical profiles of IIVP_storm for 9 km^2, (b) average vertical profiles of IIVP_storm for 25 km^2 grid box, (c)average vertical profiles of IIVP_storm for 49 km^2 grid box, (d) precipitation ETHs in IIVP_storm. The vertical arrow is drawn at 20 dBZ to indicate the intense convective activity, as 20 dBZ altitude represents thunderstorm activity.

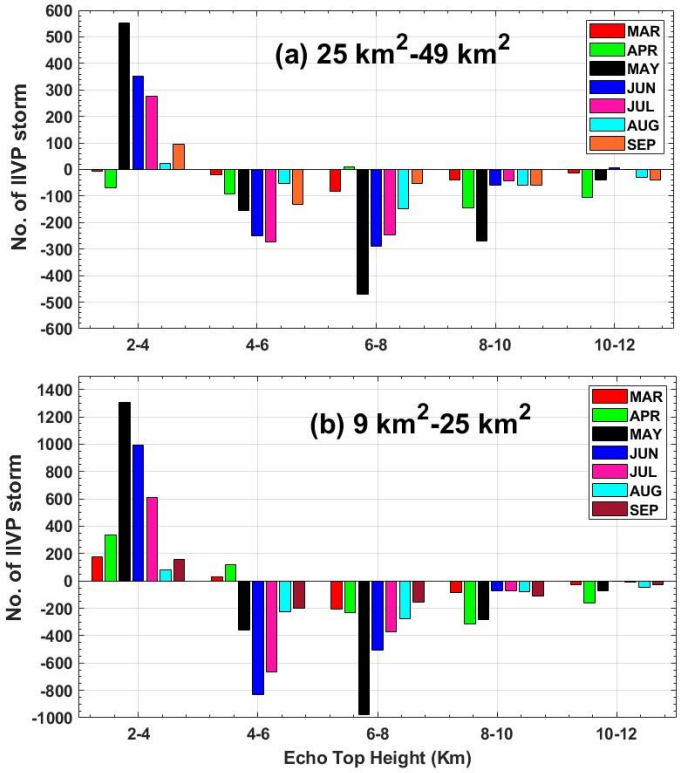

Figure 11. Difference in IIVP_storm reaching at different altitudes at different horizontal extension.

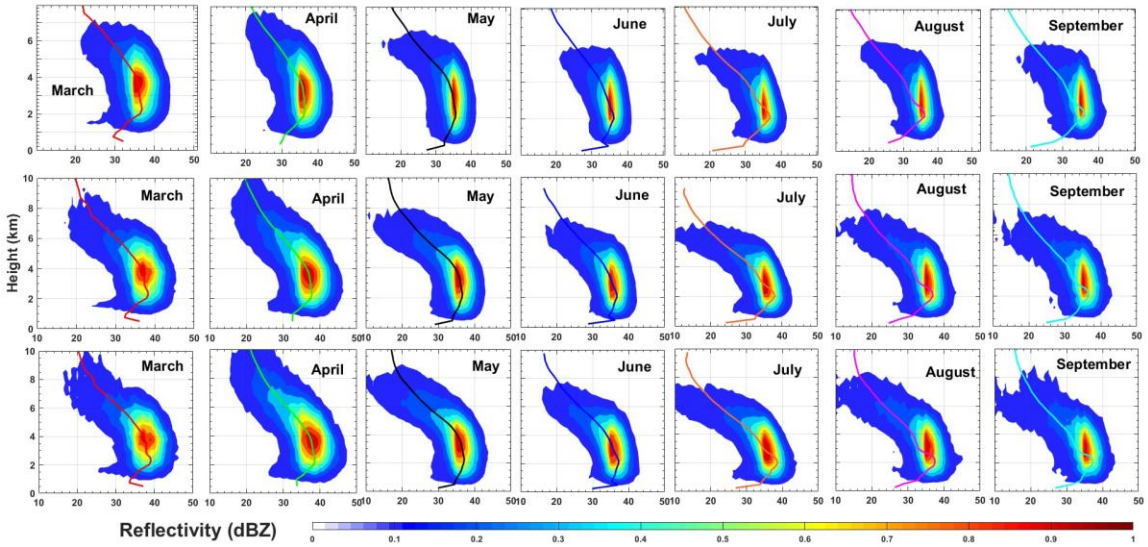

Figure 12. Contoured frequency by altitude diagram (CFAD) of Vertical profiles of IIVP_storm used in the present study. The colorbar represents the probability of Ze at the particular height. Top row: 9-km^2 grid box, middle row: 25-km^2, bottom row: 49-km^2.

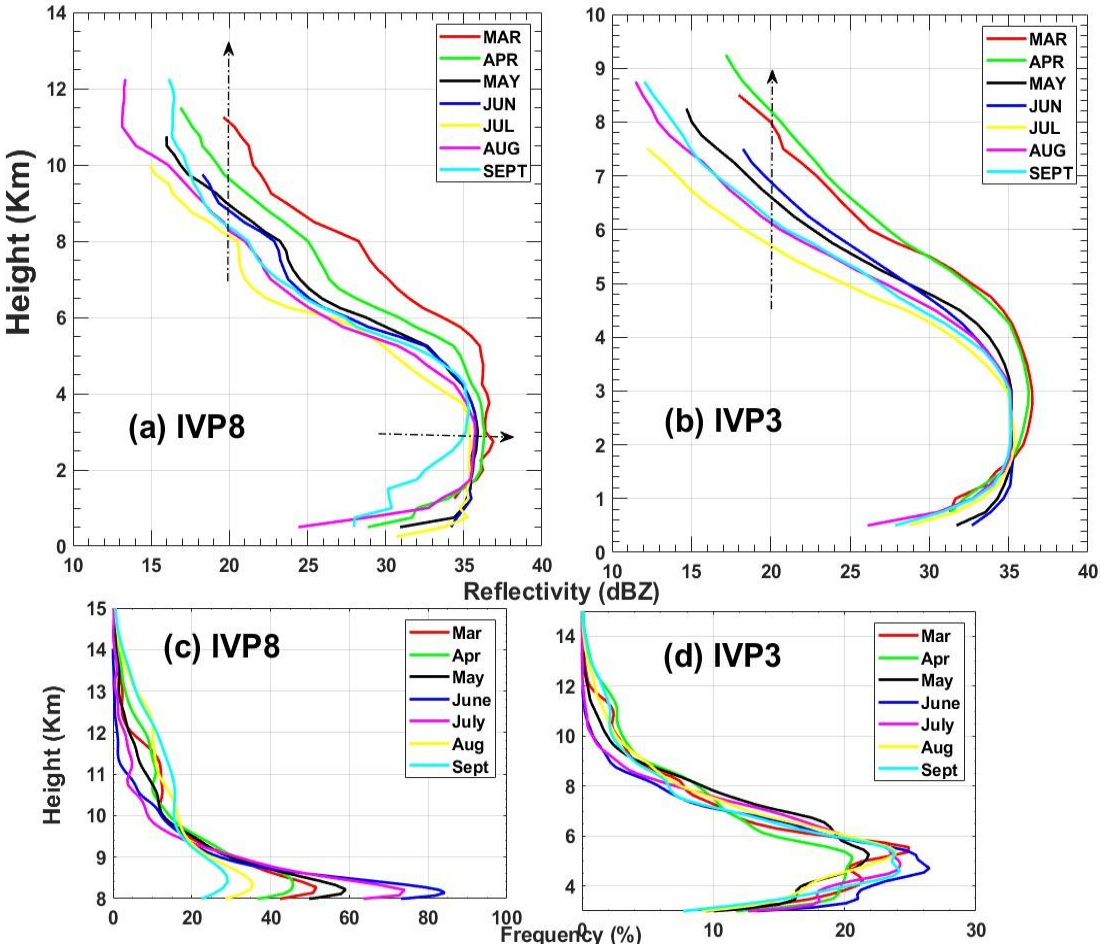

Figure 13. (a) Average vertical profiles of radar reflectivity for (a) IVP8s and (b) IVP3s. The average and median profiles are shown at the altitude where at least 90% of profiles contribute. ETHs in km for IVP8s (c) and IVP3s (d).

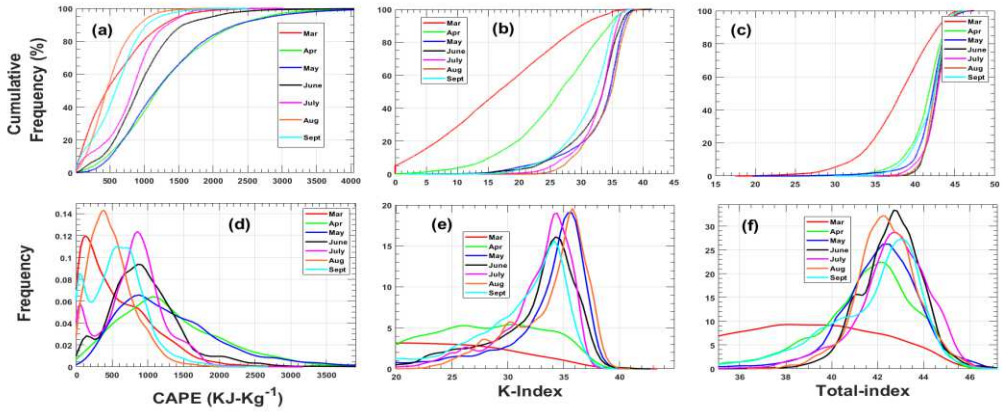

Figure 14: (a) Cumulative frequency distribution of CAPE (in KJ-Kg^{-1}) during different months, (b) Cumulative frequency distribution of K-index during different months, (c) Cumulative frequency distribution of Totals total index during different months, (d) Frequency distribution of CAPE (in KJ-Kg^{-1}) during different months, (e) Frequency distribution of K-index during different months, (f) Frequency distribution of Totals total index during different months.

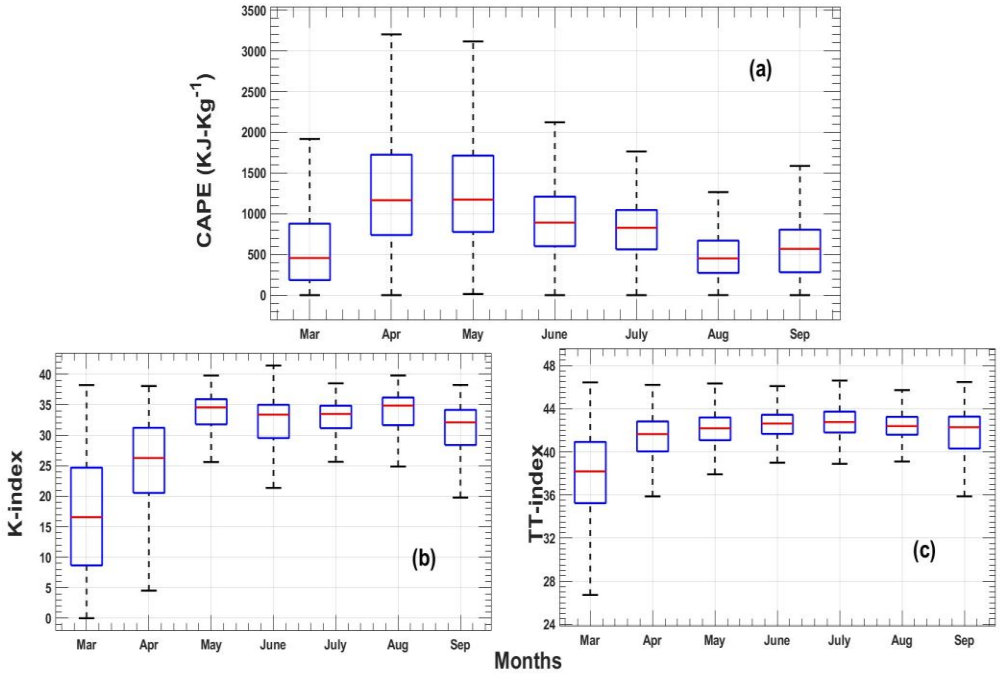

Figure 15: Boxplot of CAPE (in KJ-Kg^{-1}) during different months, (b) Boxplot of K-index during different months, (c) Boxplot of Totals total index during different months

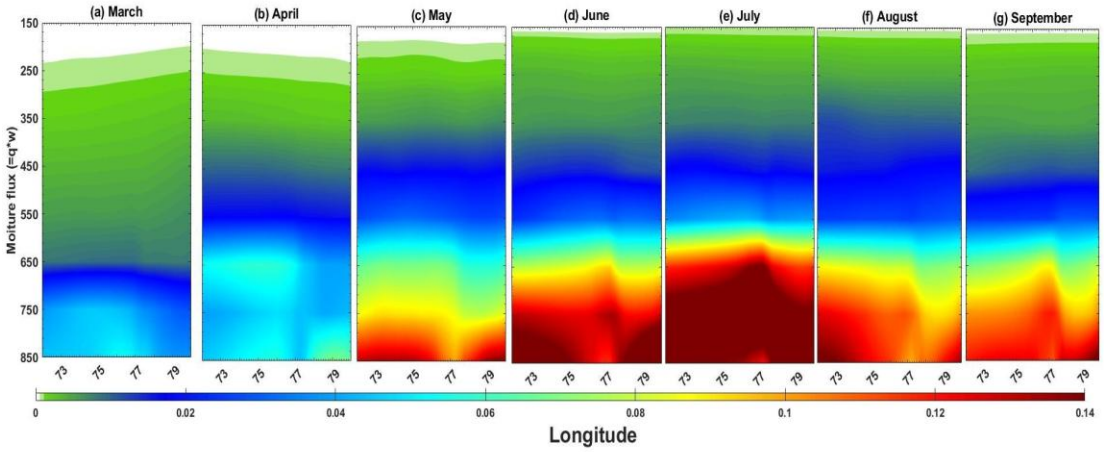

Figure 16: Meridional-pressure variation of moisture flux between 6^0 to 11^0 latitude during different months during the study periods. The colorbar represents the moisture fluxes derived from the specific humidity and wind components.

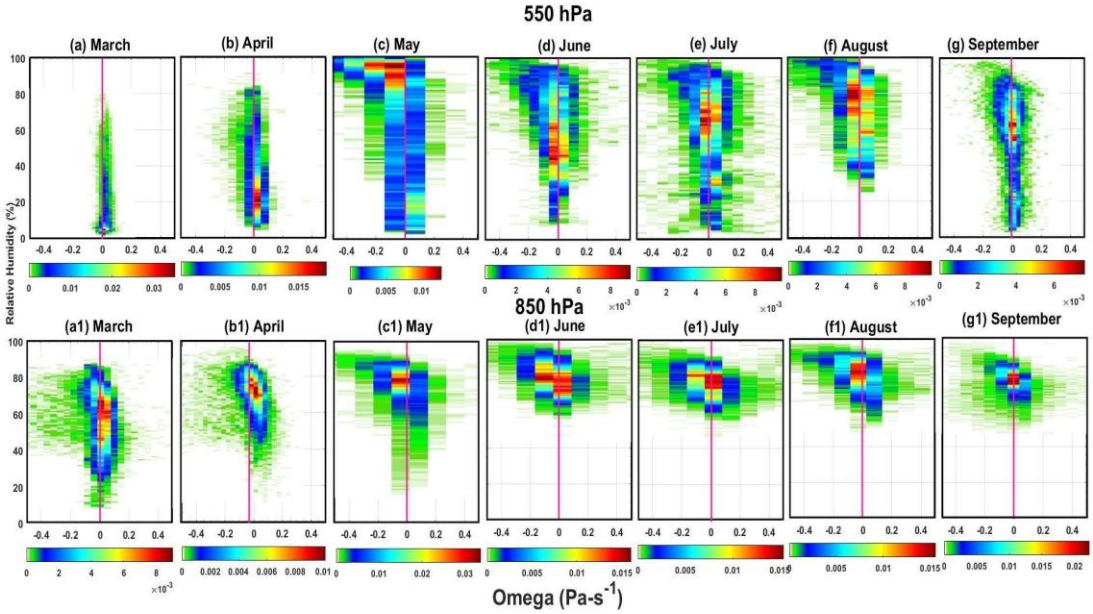

Figure 17: A joint histogram between RH (%) and vertical velocity (Omega in Pa-s^{-1}) at 550 hPa (top row) and 850 hPa (bottom row) during the study periods and study areas. The colorbar shows the relative frequencies of RH-*w* occurrence across different months using ERA data.

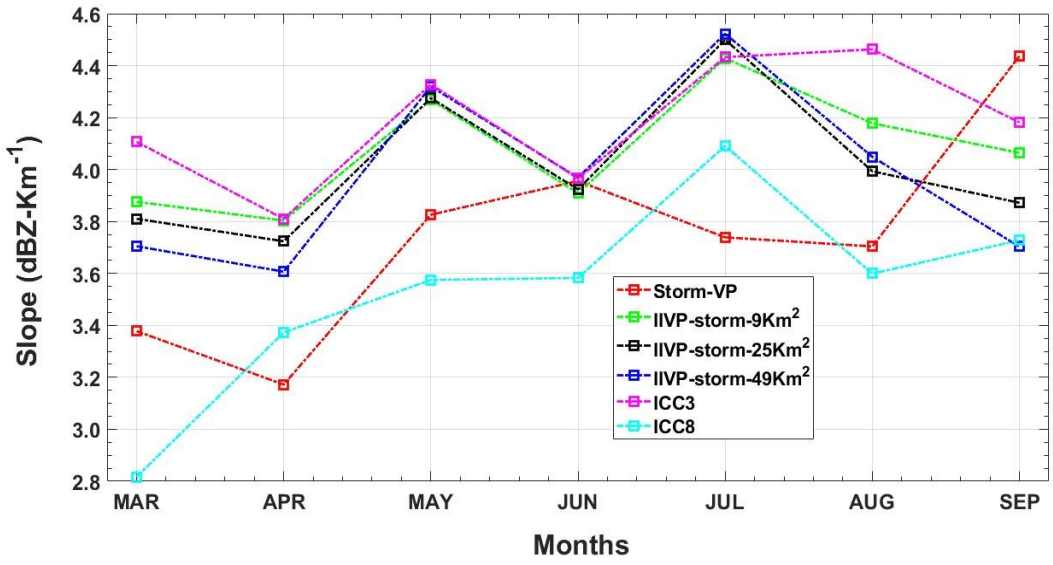

Figure 18: Radar-reflectivity slopes (dBZ-km^{-1}) between 5 to 7 Km altitude for different types of the vertical storms profiles.

Acknowledgements

The author sincerely thanks the Scientists/Engineers of Vikram Sarabhai Space Centre for providing the Doppler Weather Radar data through https://www.mosdac.gov.in and ERA5 reanalysis data team from https://www.ecmwf.int. The authors also thank both the anonymous reviewers for their valuable suggestions and comments.

Author contributions

Shailendra Kumar: Conceptualization, Methodology, Formal Analysis, Writing-Original Draft, Data curation, formal analysis, writing, review, and editing.

Data availability

DWR data can be obtained from www.mosdac.gov. in. ERA5 reanalysis fromhttps://cds.climate.copernicus.eu/cdsapp#!/ dataset/reanalysis-era5.

Reference

Bhat, G. S., and Shailendra Kumar. "Vertical structure of cumulonimbus towers and intense convective clouds over the South Asian region during the summer monsoon season." *Journal of Geophysical Research: Atmospheres* 120, no. 5 (2015): 1710-1722.

Bipasha Paul Shukla, Prashant Kumar Saxena and Sambit Kumar Panda, Study of Tropical cyclone Okchi using TERLS DWR, SAC Report, SAC/EPSA/TDP/SR/09/2018

Basu BK (2007) Diurnal variation in precipitation over India during the summer monsoon season: observed and model predicted. Mon Weather Rev 135(6):2155–2167.

Caine S, Lane TP, May PT, Jakob C, Siems ST, Manton MJ, Pinto J (2013) Statistical assessment of tropical convection-permitting model simulations using a cell-tracking algorithm. Mon Weather Rev 141:557–581

Davis CA, Manning KW, Carbone RE, Trier SB, Tuttle JD (2003) Coherence of warm-season continental rainfall in numerical weather prediction models. Mon Weather Rev 131:2667–2679

Das SK, Konwar M, Chakravarty K, Deshpande SM (2017) Raindrop size distribution of different cloud types over the Western Ghats using simultaneous measurements from micro-rain radar and disdrometer. Atmos Res 186:72–82.

Dixon M, Wiener G (1993) Titan: thunderstorm identification, tracking, analysis, and nowcasting—A radar-based methodology. J Atmos Ocean Technol 10(6):785–797

Donaldson Jr, R. J. (1961). Radar reflectivity profiles in thunderstorms. *Journal of Atmospheric Sciences*, *18*(3), 292-305.

Findlater, J., 1969. A major low-level air current near the Indian Ocean during the northern summer. Q. J. R. Meteorol. Soc. 95 (404), 362–380.

Gambheer A, Bhat G (2001) Diurnal variation of deep cloud systems over the Indian region using INSAT-1B pixel data. Meteorol Atmos Phys 78:215–225.

Gambheer, Arvind V., and G. S. Bhat. "Life cycle characteristics of deep cloud systems over the Indian region using INSAT-1B pixel data." *Monthly weather review* 128, no. 12 (2000): 4071-4083.

Gianfranco Vulpiani, and Coauthors, 2012: On the use of dual-polarized c-band radar for operational rainfall retrieval in mountainous areas. J. Appl. Meteor., 51(2):405–425.

Goudenhoofdt E, Delobbe L (2013) Statistical characteristics of convective storms in Belgium derived from volumetric weather radar observations. J Appl Meteorol Climatol 52(918):934.

George JJ. Weather forecasting for aeronautics. Academic press. 2014

Grieser J. Convection parameters. Selbstverl. 2012

Gray, W. M. and R。W。Jacobson, 1977 .Diumal variation of deep cumulus convention. Mon. Weather Rev. , 105, 1171-1188.

Guimond, S. R., G. M. Heymsfield, and F. J. Turk (2010), Multiscale observations of hurricane Dennis (2005): The effect of hot towers on rapid intensification, *J. Atmos. Sci.*, 67, 633–654

Hersbach, H., Bell, B., Berrisford, P., Biavati, G., Horányi, A., Muñoz Sabater, J., Nicolas, J., Peubey, C., Radu, R., Rozum, I., Schepers, D., Simmons, A., Soci, C., Dee, D., Thépaut, J-N. (2023): ERA5 hourly data on single levels from 1940 to present. Copernicus Climate Change Service (C3S) Climate Data Store (CDS), DOI:10.24381/cds.adbb2d47

Heymsfield, G. M., L. Tian, A. J. Heyms"eld, L. Li, and S. Guimond (2010), Characteristics of deep tropical and subtropical convection from nadir-viewing high-altitude airborne Doppler radar, J. Atmos. Sci., 67, 285–308.

Houze RA (2004) Mesoscale convective systems. Rev Geophys 42: RG4003.

Houze, R. A., Jr., D. C. Wilton, and B. F. Smull. 2007. “Monsoon Convection in the Himalayan Region as Seen by the TRMM Precipitation Radar.” Quarterly Journal of the Royal Meteorological Society 133, no. 627: 1389–1411.

Jha AK, Das SK, Deshpande SM, Murali Krishna UV (2021) Understanding the relationship of storm-to large-scale environment in the monsoon trough region: results inferred from long-term radar and reanalysis datasets. Q J R Meteorol Soc 148(742):97–116.

Jha AK, Das SK, Krishna UVM, Deshpande SM (2022) Role of thermodynamics and dynamics in the diurnal cycle, propagation, and progression of convective storms in the eastern flank of the Indian monsoon trough. J Atmos Sci 79(12):3351–3374.

Jha AK, Das SK, Deshpande SM, Murali Krishna UV (2023) Radar observed convective storm characteristics at the eastern edge of the Indian summer monsoon trough. Clim Dyn 61(7):3633–3652.

Joseph, P. and Sijikumar, S.: Intraseasonal variability of the low- level jet stream of the Asian summer monsoon, J. Climate, 17, 1449–1458, 2004.

Jorgensen, David P., and Margaret A. LeMone. "Vertical velocity characteristics of oceanic convection." *Journal of Atmospheric Sciences* 46, no. 5 (1989): 621-640.

Koteswaram, P., 1958. The easterly jet stream in the tropics. Tellus 10 (1), 43–57.

Kumar S, Bhat GS (2016) Vertical profiles of radar reflectivity factor in intense convective clouds in the tropics. J Appl Meteorol Climatol.

Kumar KK, Subrahmanyam KV, Kumar CP, Shanmugasundari J, Koushik N, Ajith RP, Girija Devi L (2020) C-band dual-polarization Doppler weather radar at THUMBA (8.537° N, 76.865° E): initial results and validation. J Appl Remote Sens 14(4):044509– 044509.

Krishna, U.M., Das, S.K., Deshpande, S.M. and Pandithurai, G., 2021. Physical processes controlling the diurnal cycle of convective storms in the Western Ghats. *Scientific Reports*, *11*(1), p.14103.

Kumar, Shailendra. "Differences in the convective variability during active and break spells over South Asian region using 25 years of satellite observations and reanalysis data: S. Kumar." *Theoretical and Applied Climatology* 156, no. 7 (2025): 415.

Kumar, S., 2025. Precipitation Structure and Convective Intensity Over South-East South Asia During Active and Break Spells of the Indian Summer Monsoon Using TRMM, GPM, Megha-Tropiques Satellites and Reanalysis Data. *International Journal of Climatology*, *45*(5), p.e8758.

Kumar, S., 2024. Regional differences in cloud characteristics at different depth, intensity and horizontal scale over South Asia during Indian summer monsoon using CloudSat and reanalysis data. *Theoretical and Applied Climatology*, *155*(12), pp.10089-10116.

Kumar, Shailendra. "Investigation of radar reflectivity profiles below the freezing level over South East South Asia using TRMM and Megha-Tropiques satellites." *Remote Sensing Letters* 15, no. 12 (2024): 1250-1258

Kumar, Shailendra. "Regional and seasonal differences of radar reflectivity slopes in lower troposphere in convective and stratiform precipitation using TRMM PR data." *Theoretical and Applied Climatology* 155, no. 4 (2024): 2719-2728.

Kumar, Shailendra, Jose Luis Flores-Rojas, Aldo S. Moya-Álvarez, Daniel Martínez-Castro, and Yamina Silva. "Hydrometeors distribution in intense precipitating cloud cells over the earth's during two rainfall seasons." *Journal of the Indian Society of Remote Sensing* 52, no. 1 (2024): 95-111.

Kumar, Shailendra, and Yamina Silva. "Distribution of hydrometeors in monsoonal clouds over the South American continent during the austral summer monsoon: GPM observations." *International Journal of Remote Sensing* 41, no. 10 (2020): 3677-3707.

Kumar, S., and Y. Silva. "Distribution of hydrometeors in intense convective clouds over South America during Austral summer monsoon seasons: GPM observations." *International Journal of Remote Sensing* 41 (2020): 3677-3707.

Kumar, Shailendra, and Yamina Silva. "Vertical characteristics of radar reflectivity and DSD parameters in intense convective clouds over South East South Asia during the Indian Summer monsoon: GPM observations." *International Journal of Remote Sensing* 40, no. 24 (2019): 9604-9628.

Kumar, Shailendra, Yamina-Silva Vidal, Aldo S. Moya-Álvarez, and Daniel Martínez-Castro. "Effect of the surface wind flow and topography on precipitating cloud systems over the Andes and associated Amazon basin: GPM observations." *Atmospheric Research* 225 (2019): 193-208.

Kumar, Shailendra, Yamina Silva, Aldo S. Moya-Alvarez, and Daniel Martínez-Castro. "Seasonal and regional differences in extreme rainfall events and their contribution to the world's precipitation: GPM observations." *Advances in Meteorology* 2019, no. 1 (2019): 4631609.

Kumar, Shailendra. "Vertical structure of precipitating shallow echoes observed from TRMM during Indian summer monsoon." *Theoretical and applied climatology* 133, no. 3 (2018): 1051-1059.

Kumar, Shailendra, and G. S. Bhat. "Vertical structure of orographic precipitating clouds observed over south Asia during summer monsoon season." *Journal of Earth System Science* 126, no. 8 (2017): 114.

Kumar, S. and Bhat, G.S. (2016) Vertical profiles of radar reflectivity factor in intense convective clouds in the Tropics. *Journal of Applied Meteorology and Climatology*, 55, 1277–1286

Kumar, Shailendra. "A 10-year climatology of vertical properties of most active convective clouds over the Indian regions using TRMM PR." *Theoretical and applied climatology* 127, no. 1 (2017): 429-440.

Kumar, Shailendra. "Three dimensional characteristics of precipitating cloud systems observed during Indian summer monsoon." *Advances in Space Research* 58, no. 6 (2016): 1017-1032.

Kumar, Shailendra, and G. S. Bhat. "Vertical profiles of radar reflectivity factor in intense convective clouds in the tropics." *Journal of Applied Meteorology and Climatology* 55, no. 5 (2016): 1277-1286.

LeMone, M. A., and E. J. Zipser (1980), Cumulonimbus vertical velocity events in GATE: Part I. Diameter, intensity, and mass !ux, J. Atmos. Sci., 37, 2444–2457.

Liu, C., and E. J. Zipser. 2015. “The Global Distribution of Largest, Deepest, and Most Intense Precipitation Systems.” Geophysical Research Letters 42: 3591–3595.

Lucas, C., E. J. Zipser, and M. A. LeMone. 1994. “Vertical Velocity in Oceanic Convection Off Tropical Australia.” Journal of the Atmospheric Sciences 51: 3183–3193

Marco Gabella and Riccardo Notarpietro, 2002: Ground clutter characterization and elimination in mountainous terrain. In Use of radar observations in hydrological and NWP models, Katlenburg-Lindau, Copernicus, 305–311.

Mathew, Thara Anna, Neelam Malap, M. G. Manoj, Y. Jayarao, Kiran Todekar, V. Rakesh, Rejoy Rebello, K. Mohankumar, and Thara Prabhakaran. "Pre-monsoon convective events and thermodynamic features of southwest monsoon onset over Kerala, India–A case study." *Atmospheric Research* 248 (2021): 105218.

Miller RC. Notes on analysis and severe-storm forecasting procedures of the Military Weather Warning Center (Vol. 200). Air Weather Service (MAC), United States Air Force. 1967

Mohanty, U.C., Dube, S.K., Singh, M.P., 1983. A study of heat and moisture budget over the Arabian Sea and their role in the onset and maintenance of summer monsoon. J. Meteor. Soc. Japan 61 (2), 208–221.

Nesbitt, S. W., E. J. Zipser, and D. J. Cecil (2000), A census of precipitation features in the tropics using TRMM radar, ice scattering, and lightning observations, J. Clim., 13, 4087–4106.

Nesbitt, S. W., R. Cifelli, and S. A. Rutledge (2006), Storm morphology and rainfall characteristics of TRMM precipitation features, Mon. Weather Rev., 134, 2702–2721.

Nesbitt, S. W., R. Cifelli, S. A. Rutledge, D. J. Boccippio, D. J. Cecil, and E. J. Zipser. 2004. "The Horizontal Structure of Precipitating Systems in the Tropics According to TRMM." Preprint 2.

Nesbitt, S. W., and E. J. Zipser. 2003. "The Diurnal Cycle of Rainfall and Convective Intensity According to Three Years of TRMM Measurements." Journal of Climate 16, no. 10: 1456–1475.

Nesbitt, S. W., E. J. Zipser, and D. J. Cecil. 2000. "A Census of Precipitation Features in the Tropics Using TRMM: Radar, Ice Scattering, and Lightning Observations." Journal of Climate 13, no. 3: 4087–4106.

Novo S, Martínez D, Puentes O (2014) Tracking, analysis, and nowcasting of Cuban convective cells as seen by radar. Meteorol Appl 21:585–595

Potts RJ, Keenan TD, May PT (2000) Radar characteristics of storms in the Sydney area. Mon Weather Rev 128(9):3308–3319.

Qie, X. S., X. K. Wu, T. Yuan, J. C. Bian, and D. R. Lu. 2014. "Comprehensive Pattern of Deep Convective Systems Over the Tibetan Plateau-South Asian Monsoon Region Based on TRMM Data." Journal of Climate 27: 6612–6626.

Romatschke U, Houze RA (2011a) Characteristics of precipitating convective systems in the South Asian monsoon. J Hydrometeorol 12:3–26.

Romatschke U, Houze RA (2011b) Characteristics of precipitating convective systems in the pre-monsoon season of South Asia. J Hydrometeorol 12(2):157–180.

Sambit Kumar Panda, Bipasha Paul Shukla, and Prashant Kumar, Clutter Mitigation and 3D volumetric gridding of TERLS DWR Reflectivity Data (V1.0), SAC Report,

Sindhu KD, Bhat GS (2018) Characteristics of monsoonal precipitating cloud systems over the Indian subcontinent derived from weather radar data. Q J R Meteorol Soc 144:1742–1760.

Sindhu KD, Bhat GS (2019) Storm characteristics and precipitation estimates of monsoonal clouds using C-band polarimetric radar over Northwest India. Theor Appl Climatol 138:237–248.

Sindhu KD, Bhat GS (2021) Seasonal characteristics of storms over the Indian subcontinent. Sci Rep 11(1):3355.

Sindhu and Bhat (2018) Characteristics of monsoonal precipitating cloud systems over the Indian subcontinent derived from weather radar data*Q J R Meteorol Soc.* 2018;144:1742–1760.

Sindhu and Bhat (2019) Storm characteristics and precipitation estimates of monsoonal clouds using C-band polarimetric radar over Northwest India. Theoretical and Applied Climatology (2019) 138:237–248

Shah S, Notarpietro R, Branca M (2015) Storm identification, tracking and forecasting using high-resolution images of short-range X-band radar. Atmosphere 6:579-606

Szoke, Edward J., Edward J. Zipser, and David P. Jorgensen. "A radar study of convective cells in mesoscale systems in GATE. Part I: Vertical profile statistics and comparison with hurricanes." *Journal of Atmospheric Sciences* 43, no. 2 (1986): 182-198.

Subrahmanyam KV, Kumar KK (2022a) C-band polarimetric doppler weather radar observations during an extreme precipitation event and associated dynamics over Peninsular India. Nat Hazards 114(2):1307–1322.

Subrahmanyam KV, Kumar KK (2022b) Structure and evolution of organized precipitation bands: C-band doppler weather radar observations over THUMBA. Atmosph Res 284(2022):10659.

Subrahmanyam KV, Kumar KK (2023) Characterization of deep convective cells during the Indian summer monsoon using C-band polarimetric Doppler Weather Radar observations over THUMBA (8.5 o N, 77o E). Remote Sens Appl Soc Environ 30:100956.

Thomas, Lois, Neelam Malap, Wojciech W. Grabowski, Kundan Dani, and Thara V. Prabha. "Convective environment in pre-monsoon and monsoon conditions over the Indian subcontinent: the impact of surface forcing." *Atmospheric Chemistry and Physics* 18, no. 10 (2018): 7473-7488.

Uma, K.N. and Sama, B., 2025. Characteristics of monsoon convection and its interaction with the large-scale environment over the gateway of the Indian summer monsoon: insights from radar observations and reanalysis. *Climate Dynamics*, *63*(10), p.379.

Utsav B, Deshpande SM, Das SK, Pandithurai G (2017) Statistical characteristics of convective clouds over the western ghats derived from weather radar observations. J Geophys Res Atmos 122:10050–10076.

Utsav B, Deshpande SM, Das SK, Pandithurai G, Niyogi D (2019) Observed vertical structure of convection during dry and wet summer monsoon epochs over the Western Ghats. J Geophys Res Atmos 124(3):1352–1369.

Virts, K.S. and Houze Jr, R.A., 2016. Seasonal and intraseasonal variability of mesoscale convective systems over the South Asian monsoon region. *Journal of the Atmospheric Sciences*, *73*(12), pp.4753-4774.

Xu, W., and E. J. Zipser. 2012. “Properties of Deep Convection in Tropical Continental, Monsoon, and Oceanic Rainfall Regimes.” Geophysical Research Letters 39, no. 7.

Zhang et al. 2006, An Automated 2D Multipass Doppler Radar Velocity Dealiasing Scheme, J. of Atmos. And Ocean Tech, 23, 1239-1248, 2006

Zipser EJ, Lutz KR (1994) The vertical profile of radar reflectivity of convective cells: a strong indicator of storm intensity and lightning probability? Mon Weather Rev 122:1751–1759

Zipser EJ, Cecil D, Liu C, Nesbitt S, Yorty D (2006) Where are the most intense thunder storms on earth? Bull Am Meteorol Soc 87:1057– 1071.

Month/grid size	MAR	APR	MAY	JUN	JUL	AUG	SEPT
1-km (9 km^2)	16833	43749	49488	32968	28131	21121	13864
2-km (25 km^2)	12082	31739	36121	24894	21025	16237	10484
3-km (49 km^2)	9412	24537	28821	20567	17490	13615	8791

Table-1 shows the number of the profiles (IIVP_storm) observed at different horizontal scales and it is seen that April and May have the highest number of IIVP_storm, whereas September has the least frequent IIVP_storm.

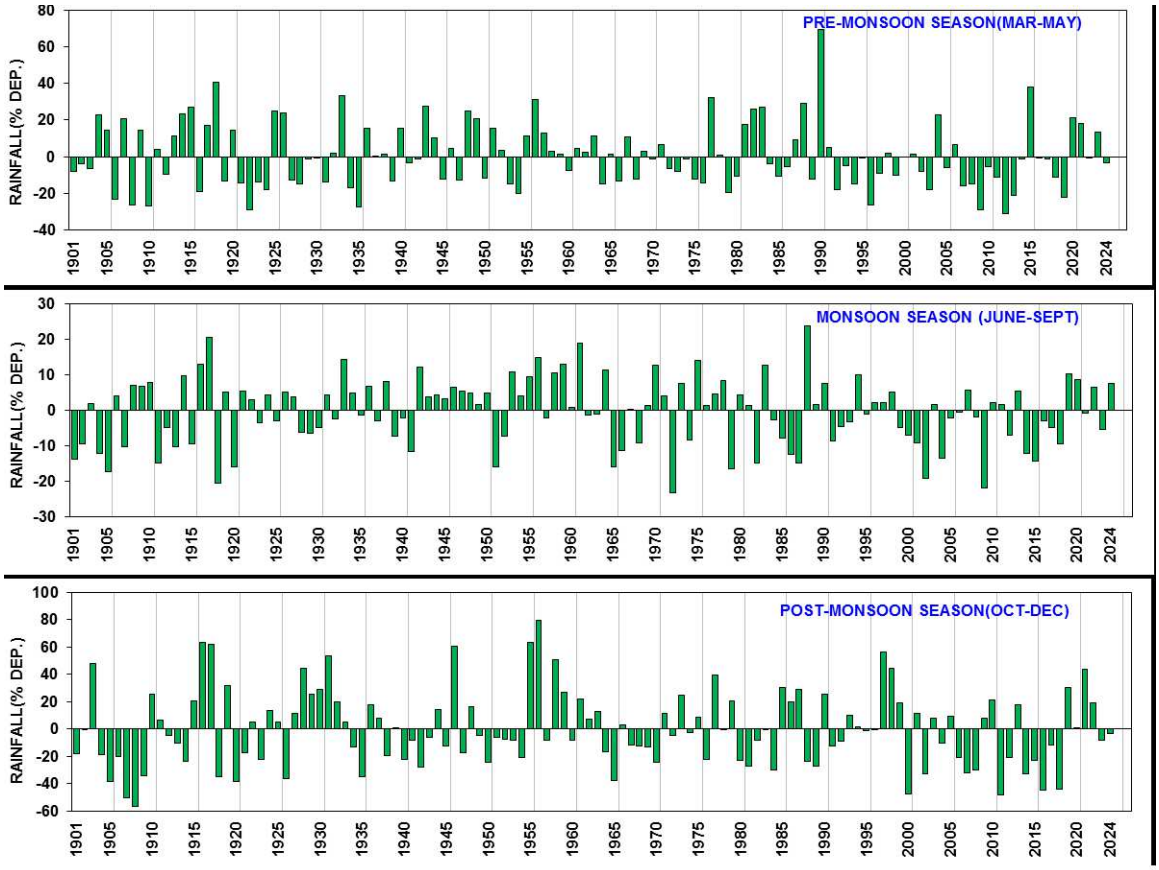

Suplementary Figure 1. Percentage departure of area weighted (Seasonal and Annual) rainfall over the country as a whole for 1901-2024. (Climatology period 1971-2020 (Source: Indian Meteorological Department))

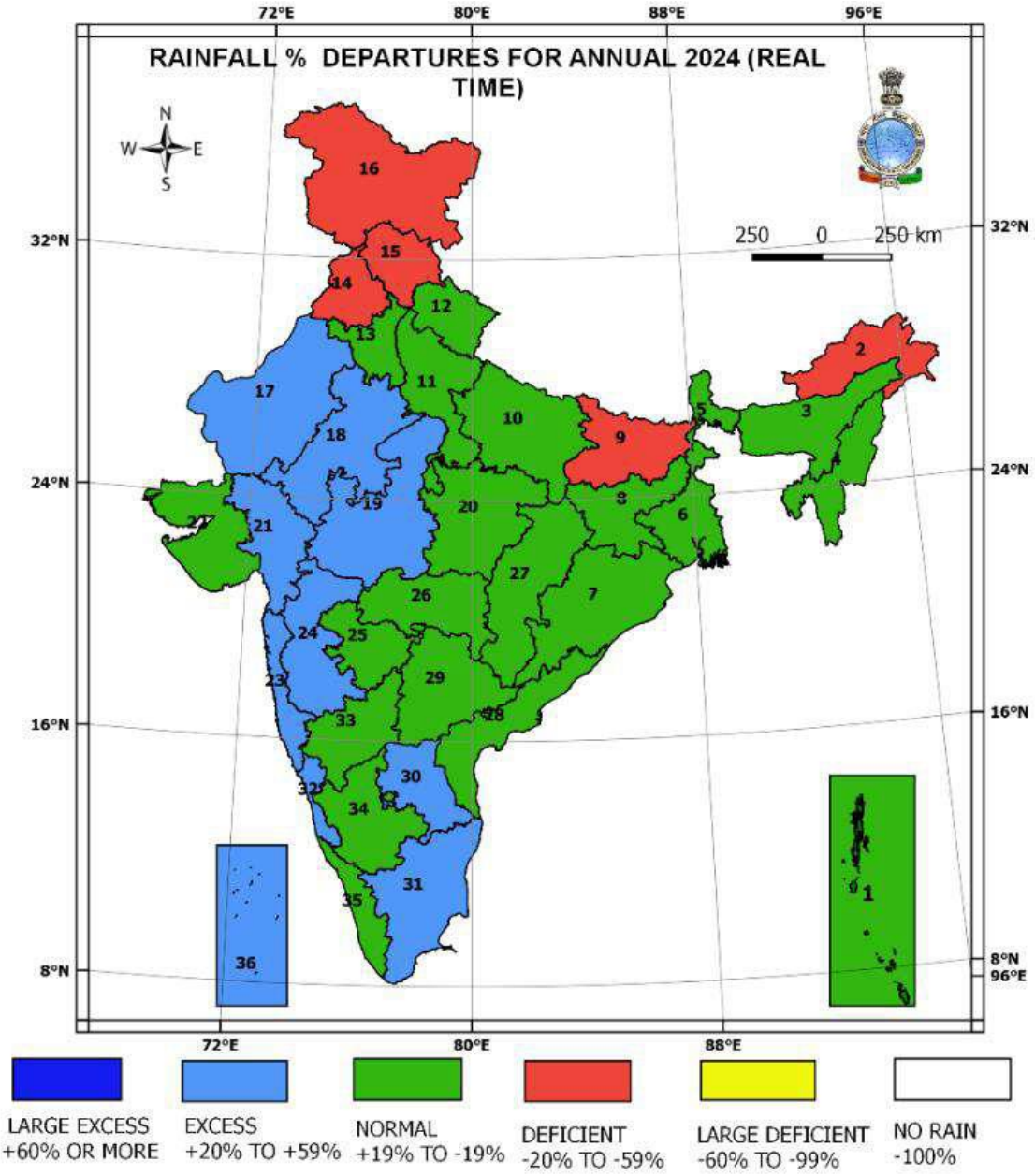

Suplementary Figure 2. Sub-division-wise Annual rainfall percentage departure for 2024 (Source: Indian Meteorological Department).